On the Structure of Ionic Liquids: Comparisons between Electronically Polarizable and Nonpolarizable Models I

Tianying Yan,*,† Yanting Wang,‡ and Craig Knox§

Institute of New Energy Material Chemistry and Department of Material Chemistry, Nankai University, Tianjin 300071, China, Key Laboratory of Frontiers in Theoretical Physics, Institute of Theoretical Physics, Chinese Academy of Sciences, 55 East Zhongguancun Road, Beijing, 100190, China, and Center for Biophysical Modeling and Simulation and Department of Chemistry, University of Utah, Salt Lake City, Utah 84112-0850

Received: September 15, 2009; Revised Manuscript Received: April 1, 2010

An electronically polarizable model, based on the AMBER nonpolarizable model, has been developed for the ionic liquid (IL) 1-ethyl-3-methyl-imidazolium nitrate ($EMIM^+/NO_3^-$). Molecular dynamics simulation studies were then performed with both the polarizable and nonpolarizable models. These studies suggest $EMIM^+$ cations have a strong tendency to pack with their neighboring imidazolium rings nearly parallel to each other, bridged by hydrogen bonds to NO_3^- anions. Polarization has two key effects, (1) additional charge−dipole and dipole−dipole interactions enhance short-range electrostatic interactions and (2) screening reduces long-range electrostatic interactions. As a result, the polarizable model exhibited enhanced hydrogen bonding compared to the nonpolarizable model, while the latter retained more ordered long-range spatial correlations than the former. Though $EMIM^+$ has a very short nonpolar ethyl tail group, spatial heterogeneity, previously observed with long-chain ILs, was observed in this system and has been quantified using the heterogeneity order parameter. The polarizable model was slightly more heterogeneous than the nonpolarizable model. The enhanced spatial heterogeneity of the polarizable model is again attributed to the stronger short-range electrostatic interactions, which "push" the nonpolar tails away from the polar heads, leading to more aggregation and a strongly altered ionic packing pattern around NO_3^- as observed by a different anion−anion center-of-mass partial radial distribution function $g_{--}(r)$. Interestingly, both models seemed to "remember" the crystal structure even at temperatures significantly higher (∼90 K higher) than the melting point (311 K). Along with the results on the dynamical properties reported in the accompanying paper, the current study demonstrates that electronic polarizability is significant in ionic liquid systems.

I. Introduction

Room temperature molten salts (RTMS), or ionic liquids (ILs), have recently stimulated a significant body of research. Like inorganic molten salts, ILs are composed solely of ions, but in contrast, their melting point is often less than 100 °C. There are potentially on the order of millions of varieties of ILs, but most ILs of recent interest are based on nitrogen-rich alkyl-substituted heterocyclic cations, accompanied with different kinds of inorganic anions. Because of their "green" properties, such as low volatility, nonflammability, reusability, and selectivity, ILs are actively explored as possible substitutes for conventional organic solvents in a variety of electrochemical, synthetic, and separation processes. Despite the current level of research activity, many properties of these interesting liquids remain to be elucidated.[1] For a comprehensive review of the physicochemical properties of ILs, we refer to the review articles[2] as well as recent accounts.[3]

Recently, rich amounts of information on the structural properties of this new class of liquid have been explored. Hardacre and co-workers performed neutron diffraction studies on the structural properties of a variety of ILs, including 1,3-dimethylimidazolium chloride ($DMIM^+/Cl^-$),[4,5] 1,3-dimethylimidazolium hexafluorophosphate ($DMIM^+/PF_6^-$),[4,5] 1,3-dimethylimidazolium bis(trifluoromethane sulfonyl)imide ($DMIM^+/TFSI^-$),[6] and 1-methyl-4-cyano-pyridinium bis(trifluoromethane sulfonyl)imide.[7] The experimental differential cross sections were then subjected to the empirical potential structure refinement (EPSR)[8] process using Monte Carlo trial moves with an empirical forcefield developed by Lynden-Bell and co-workers[9] to produce the best fit to the diffraction data and to extract the center-of-mass partial radial distribution functions (PRDFs) as well as other structural properties, including iso-density spatial distribution functions. These studies highlight the considerably short-range ordering in the liquid phase. The existence of hydrogen bonding networks in room temperature ionic liquids has been verified by several experimental studies on the crystal,[10,11] glass,[12] and liquid states,[4,5,13] as well as by computer simulations.[9,14] For the imidazolium-based ILs, the strongest hydrogen bond is associated with the most acidic hydrogen atom (H2),[15] followed by H4 and H5 (cf. Figure 1).

The IR spectra of $EMIM^+/AlCl_4^-$[16] in the liquid phase shows a Cl^- interaction band between Cl^- and H2, H4, and H5 atoms on the imidazolium ring. Theoretical calculations using semiempirical,[16] density functional theory (DFT),[17] and high-level ab initio[18] methods suggest a high probability of hydrogen bond formation between anions and the ring H-atoms (H2, H4, and H5). The pressure-dependent IR frequency shift, attributed to the enhanced C−H---X^- hydrogen bonding, also demonstrates that the H-atoms attached to the imidazolium ring are the

* To whom correspondence should be addressed. Tel: (86)22-23505382. Fax: (86)22-23502604. E-mail: tyan@nankai.edu.cn.
† Nankai University.
‡ Chinese Academy of Sciences.
§ University of Utah.

10.1021/jp9089112 © 2010 American Chemical Society
Published on Web 05/05/2010

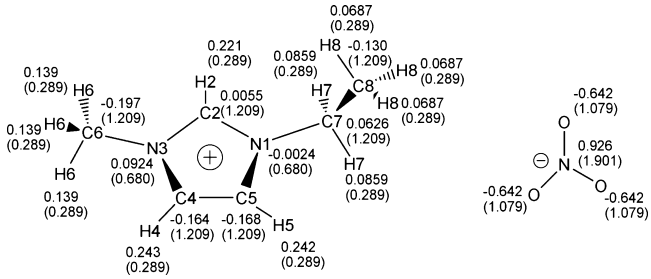

Figure 1. The RESP fitted partial charges and atomic polarizabilities (in parentheses) for $EMIM^+$ and NO_3^-. The polarizability is fit to Thole's smearing dipole model with the smearing factor $a = 2.392$ in eq 2.

favorable sites to form hydrogen bonds with anions.[19] The combined IR, NMR study and ab initio calculations also highlight the importance of hydrogen bonding for the cation−anion interactions, whose corresponding intermolecular vibrational modes shift to higher frequencies with increasing ionic strength of the anions.[20] Such hydrogen bonding networks have also been demonstrated by computer simulations.[21,22] A Raman spectroscopic study of $EMIM^+$ found a 448 cm^{-1} band from the planar conformers of $EMIM^+$,[23] indicating the existence of the liquid state trans and gauche conformers, in agreement with the MD simulation study.[24−26] The Raman spectra of the $BMIM^+/Cl^-$ crystal also reveals two rotational isomers of the butyl side chain.[27] The coexistence of two conformers of the anion in the $EMIM^+/TSFI^-$ IL was also found by Raman spectroscopy and DFT calculations.[28] Such promising combinational DFT/spectroscopy studies may help systematically design functional ILs.[29]

The spatial correlation in the ionic liquid systems leads to the aggregation of the nonpolar tails due to the competition between the strong electrostatic interactions among the charged cationic head groups and the anions and the weak van der Waals interactions among the nonpolar cationic tail groups,[30−32] as first revealed by molecular dynamics simulations with the multiscale coarse-graining (MS-CG) approach.[33,34] Thus, ILs can be characterized as heterogeneous media with high- and low-charge density domains.[35] This mechanism has been verified by all-atom[26,36,37] and coarse-graining (CG)[38,39] simulations as well as experimental studies. For instance, optical heterodyne-detected Raman-induced Kerr effect spectroscopy (OHD-RIKES) indicates a tendency for the polar head groups to form a network that encloses the nonpolar region.[40] Coherent anti-Stokes Raman Scattering (CARS) spectroscopy on the total symmetric P−F stretch mode of PF_6^- of C_nMIM^+/PF_6^- (n = 4, 6, 8) reveals the formation of local structures, based on the optical inhomogeneity of ILs at the microscopic level.[41] Small-angle X-ray scattering (SAXS) on C_nMIM^+/PF_6^- (n = 6, 8, 10)[42] and trialkyl-methyl-ammonium $[N1(n)_3^+]/TFSI^-$ (n = 4, 6, 8)[43] as well as small-wide-angle X-ray scattering (SWAXS) on *N*-alkyl-*N*-methyl-piperidinium $(PIP_{1n}^+)/TFSI^-$ ($n \leq 3 \leq 7$)[44] also suggest segregation of the alkyl side-chain. A recent study with SWAXS and OHD-RIKES on $C_nMIM^+/TFSI^-$ suggested that side chain aggregation only occurs for $n \geq 3$.[45] Even ILs with short alkyl side groups, such as ethylammonium nitrate (EAN), exhibit this behavior, according to small-angle neutron scattering (SANS) spectroscopy.[46] Time-dependent fluorescence of dipolar molecules in ILs shows the "red-edge effect", which is attributed to the spatial heterogeneity of ILs.[47] Mesoscopic structure, arising from IL cluster formation, is also detected by dielectric spectroscopy.[48] Also, low-dimensional continuous ionic nanochannels, which efficiently transport ions, have been found in self-organizing ammonium-based IL in a liquid crystalline phase.[49]

The electrostatic and induction interactions contribute greatly to the stability of the cation−π stacking between aromatic cations and result in unique structure of the mixtures, as studied by both experimental[50] and ab initio[51] studies. On the other hand, despite the repulsion force between like charges, cation−cation $\pi-\pi$ stacking, in which the cations arrange in a face-to-face alignment and parallel displacement with interplanar distance 3.2−3.8 Å, was found in crystal IL 1-methylimidazolium $CF_3SO_3^-$.[52] Also, $\pi-\pi$ stacking as well as C−H−π interactions were found in crystal $EMIM^+/BF_4^-$.[53] Two-dimensional NMR nuclear overhauser effect (NOE) studies on the cation−cation distances of imidazolium-based IL clearly found close ring−ring aggregation with either parallel $\pi-\pi$ stacking or perpendicular T-shape configurations, though no conclusive statement was drawn.[54] Ab initio studies (MP2/aug-cc-pVDZ) have revealed similar $\pi-\pi$ stacking in small gas phase IL clusters between 1,2,4-triazolium cations.[55] Such $\pi-\pi$ stacking has not been found in Hartree−Fock optimized structures. Thus, electron correlation energy is essential for this aromatic $\pi-\pi$ attraction.[55] From B3LYP/6-31++G(d,p) calculation, hints of a Cl−π interaction between the Cl^- anion and the imidazolium ring were found in $BMIM^+/Cl^-$.[56] $\pi-\pi$ stacking, and its correlation with anion size and shape, has also been found in a variety of imidazolium-based ILs using classical[22,57,58] and ab initio[59] molecular dynamics simulation.

Since the pioneering work of Hanke and Lynden-Bell[9] in 2001, many computer simulations have been performed on ILs[9,24,25,57,60−65] to study their structural and dynamical properties. Most computer simulations of ILs have been based on nonpolarizable forcefields, such as the united-atom model, in which H and C atoms on the alkyl side-chain are grouped together,[9,57,62,66] forcefields with rigid C−H bond constraints,[65] and all-atom all-flexible forcefields.[61,64,67,68] Systematical developments of the forcefield parameters customized for IL systems have also been attempted.[64,65,67,69] To overcome the slow diffusivity of the ILs simulated with the conventional nonpolarizable forcefield, reduced nonunit charges were adopted in MD simulations.[61,70] Alternatively, it has been demonstrated that the nonpolarizable model with reduced Lennard-Jones interactions also give the diffusion coefficients and viscosities in good agreement with experimental diffusion coefficients and viscosities.[57,71] CG[38,72] models for ILs have also been utilized to simulate large IL systems. A MS-CG methodology for ILs has also been developed by force-matching a polarizable forcefield.[32,34,73] It is noteworthy to mention that there is a large discrepancy in the literature regarding partial charge assignments on the ILs, possibly leading to some artifacts in classical MD simulation results.[62,74,75] For a recent review of the computer simulation of imidazolium-based ILs, we refer to Hunt's,[76] Bhargava's,[77] Gray-Weale's,[78] and Maginn's[79] works. Also, the framework for the development of IL simulations was nicely summarized by Alavi and co-workers.[80]

Ab initio molecular dynamics (AIMD) simulations have also recently been performed on ILs.[15,21,59,81−83] With suitable functionals, AIMD may be the most accurate among existing simulation approaches. The AIMD simulation revealed the importance of the polarization effect in capturing the detailed structural properties of ILs.[15] Besides, the fluctuation of the electric dipole moment observed in AIMD cannot be captured by a nonpolarizable forcefield model.[83] AIMD can also serve as a standard or reference for other simulation techniques, for example, to be force-matched by a classical forcefield.[84] However, AIMD simulations are very computationally expen-

sive and, currently, can only probe very small systems (tens of ion pairs) for a very short time (several tens of picoseconds).

Strong electrostatic interactions in ILs lead to very long-ranged spatial correlations and very slow diffusion. Including electronic polarization in the simulations of inorganic molten salts often improves the agreement with experiments.[85] A convincing example of this is a simulation study of molten $ZnCl_2$ by Madden and Wilson.[86] By utilizing a polarizable model with the electronic induction on Cl^-, they found that the first maximum in the PRDF of Zn−Zn occurred at a distance 1 Å shorter than the nonpolarizable model, agreeing better with experiment. Another significant case was given by Saboungi et al.[87] in their study of binary molten salts with polarizable anions. They found that the position of the maximum in the cation−cation PRDF shifted from 4.6 Å for the nonpolarizable model to 2.48 Å for the polarizable model.

The above studies also highlight the polarization effect induced by the local environment on the particles in the system. For a molten salt, the size of cation determines the preferred coordination number, and the polarization effect is limited by high coordination number because the local cations around an anion are too symmetric to permit the induction of a multipole. On the other hand, if the local environment around an individual particle is anisotropic, the polarization effect could be important for highly polarizable particles.[88] In terms of dynamical properties of inorganic molten salts, polarization generally leads to an increase of ion mobility.[89,90] For example, a pioneering study of molten KI with a polarizable model showed that the polarization effect in the liquid state significantly increases diffusion and decreases viscosity.[91]

For ILs, it has been found in simulations,[9,15,24,25,62,64,92] electronic structure calculations,[74,93] and experiments[4,5,94] that the local environment around the ions is highly anisotropic. For such a system, the particles may not be well described as rigid bodies because their electron densities are distorted by their interactions with each other and their internal structural changes are basically a many-body effect.[95] Therefore, it is highly desirable to model these interactions using a fully polarizable forcefield.[96]

In a preliminary study,[63] we have reported the effect of electronic polarizability on the structure and dynamics of $EMIM^+/NO_3^-$. In the current study, we report the details of developing the polarizable IL model and discuss the results. Despite the slightly larger molecular polarizability in this study compared to the one fitted in our previous study,[63] the difference between the results for the two polarizable models is not significant, especially when compared to the difference between the results for the polarizable model and the nonpolarizable model. The major effect of electronic polarizability in the IL system is that the ions become more mobile in the polarizable model than in the nonpolarizable model. The methodology for developing the polarizable IL forcefield presented in this study is general and can be applied to other IL species as well.

Section II describes the development of the polarizable forcefield with an interactive atomic dipole model.[97−99] Section III presents the structural properties simulated by both the polarizable model and the nonpolarizable model. The summary is given in Section IV. The dynamical properties simulated by both models are reported in the accompanying paper.[100] The description of the polarizable model, using extended Lagrangian (ext-L) method for the induced dipoles, is presented in the Appendix. The comparisons of radial distribution functions between iteration method and ext-L method are also made in the Appendix, which shows good agreement with each other. In this and the accompanying paper,[100] the term dipole indicates the induced dipole unless otherwise mentioned.

II. Construction of the Polarizable Forcefield

II.1. Fitting Molecular Polarizability by Thole'S Smearing Dipole Model. Thole's smearing dipole model[98] may be considered the direct extension of Applequist's point dipole model[97] while successfully overcoming the problem of a diverging dipole in the latter.[98] Thole's model starts by replacing a point charge with a smearing charge. For a smearing charge q_j centered at point j, the effective charge at point i is given by $q_i = q_j\rho^f(r_{ij})$, where $\rho^f(r_{ij})$ is a fractional smearing function and $\int_v \rho^f(\boldsymbol{r})d\boldsymbol{r} = \int_0^\infty 4\pi r^2\rho^f(r)dr = 1$ for a spherical charge distribution. The fractional electric field, $\boldsymbol{E}^f$, at point i due to a unit smearing charge $\int_0^{r_{ij}} 4\pi r^2\rho^f(r_{ij})dr$ at point j, may be written as

$$\boldsymbol{E}^f(r_{ij}) = \frac{\boldsymbol{r}_{ij}}{r_{ij}^3}\int_0^{r_{ij}} 4\pi r^2\rho^f(r_{ij})dr \tag{1}$$

where $r_{ij} = |\boldsymbol{r}_i - \boldsymbol{r}_j|$, and the fractional electrostatic potential (ESP) may be written as

$$\varphi^f(r_{ij}) = -\int_\infty^{r_{ij}} dr'\frac{1}{r'^2}\int_0^{r'} dr\, 4\pi r^2\rho^f(r) = \frac{1}{r_{ij}}\int_0^{r_{ij}} 4\pi r^2\rho^f(r)dr - \int_\infty^{r_{ij}} 4\pi r\rho^f(r)dr$$

Equation 1 represents the starting point of Thole's derivation of the smearing dipole model by recognizing that the expression of $\boldsymbol{E}_{ij}^f(r_{ij})$ also holds for a unit smearing dipole at point j.[99] The next step is to estimate the smearing function $\rho^f(r)$. Thole evaluated six different $\rho^f(r)$ functions and for our study we chose the Slater type[98]

$$\rho^f(r) = \frac{1}{A^3}\frac{a^3}{8\pi}\exp\left(-\frac{ar}{A}\right) \tag{2}$$

where a is the smearing factor and $A_{ij} = (\alpha_i\alpha_j)^{1/6}$ has the unit of length, with α_i and α_j as the isotropic atomic polarizabilities of atoms i and j.

Incorporating eq 2 into eq 1, the fractional electric field is given by

$$\boldsymbol{E}_{ij}^f = \frac{\boldsymbol{r}_{ij}}{r_{ij}^3} - \frac{\boldsymbol{r}_{ij}}{r_{ij}^3}\exp\left(-\frac{ar_{ij}}{A_{ij}}\right)\sum_{n=0}^{2}\frac{1}{n!}\left(\frac{ar_{ij}}{A_{ij}}\right)^n \tag{3}$$

and the dipole field tensor is given by $\boldsymbol{T}_{ij} = \nabla_i\nabla_i\varphi^f(\boldsymbol{r}_{ij}) = -\nabla_i\boldsymbol{E}^f(r_{ij})$, that is

$$\boldsymbol{T}_{ij} = \left(\frac{3\boldsymbol{r}_{ij}\boldsymbol{r}_{ij}}{r_{ij}^5} - \frac{\boldsymbol{I}}{r_{ij}^3}\right) - \left[\frac{3\boldsymbol{r}_{ij}\boldsymbol{r}_{ij}}{r_{ij}^5}\exp\left(-\frac{ar_{ij}}{A_{ij}}\right)\sum_{n=0}^{3}\frac{1}{n!}\left(\frac{ar_{ij}}{A_{ij}}\right)^n - \frac{\boldsymbol{I}}{r_{ij}^3}\exp\left(-\frac{ar_{ij}}{A_{ij}}\right)\sum_{n=0}^{2}\frac{1}{n!}\left(\frac{ar_{ij}}{A_{ij}}\right)^n\right] \tag{4}$$

where $\boldsymbol{r}_{ij}\boldsymbol{r}_{ij}$ is the metric tensor and $\boldsymbol{I}$ is the unit tensor. The first term in eq 4, that is, $\nabla_i\nabla_i 1/r_{ij} = 3\boldsymbol{r}_{ij}\boldsymbol{r}_{ij}/r_{ij}^5 - \boldsymbol{I}/r_{ij}^3$, is the dipole field tensor for the point dipole model, while the power

expansions in the second term effectively damps $\boldsymbol{T}_{ij} \rightarrow 0$ for $r_{ij} \rightarrow 0$. Thus, the short-range dipole−dipole interaction is effectively screened. This solves the singularity problem associated with the point dipole model,[98] and is a desired feature of Thole's model for MD simulation.

The induced dipole moment $\boldsymbol{\mu}_i$ on atom i is given by

$$\boldsymbol{\mu}_i = \alpha_i[\boldsymbol{E}_i + \sum_{j=1,j\neq i}^{N} \boldsymbol{T}_{ij}\boldsymbol{\mu}_j] \quad (5)$$

where α_i is the isotropic atomic polarizability of atom i, $\boldsymbol{E}_i$ is the electric field on atom i, and $\boldsymbol{T}_{ij}$ is the dipole field tensor. Equation 5 may be rearranged to a single matrix form[97,98,101] $\boldsymbol{A\mu} = \boldsymbol{E}$, where for a molecule with N atoms, $\boldsymbol{A}$ is a $3N \times 3N$ matrix with $\boldsymbol{A}_{ii} = \alpha_i^{-1}$ and $\boldsymbol{A}_{ij} = -\boldsymbol{T}_{ij}$ being 3×3 submatrices, and $\boldsymbol{\mu}$ and $\boldsymbol{E}$ are $3N$ column vectors with x, y, and z Cartesian coordinates of each atom. Therefore, eq 5 may be rearranged as $\boldsymbol{\mu} = \boldsymbol{A}^{-1}\boldsymbol{E}$ and the molecular polarizability α_{mol} is given by[97]

$$\alpha_{\mathrm{mol}} = \sum_{i,j=1}^{N} \boldsymbol{A}_{ij}^{-1} \quad (6)$$

where $\boldsymbol{A}_{ij}^{-1}$ are the 3×3 submatrices of $\boldsymbol{A}^{-1}$. Thus, the molecular polarizability may be approximated by the isotropic atomic polarizabilities, which upon interacting with each other as represented by the second term on the right-hand side of eq 5, reproduce the anisotropic molecular polarizability.

For the IL system studied here, the molecular polarizabilities for $EMIM^+$ and NO_3^- were calculated by ab initio calculations performed with Gaussian03[102] with the MP2/aug-cc-pVDZ level of theory and basis set. Since polarizability is geometry dependent, the polarizabilities of $EMIM^+$ were calculated for three different configurations: the MP2/6-31g(d) optimized geometry with the ethyl group pointing out of the plane of the imidazolium ring as well as the cis and trans configurations in which the carbon atoms on the ethyl and methyl groups lie in the same plane of the imidazolium ring, but pointing to different directions. For NO_3^-, the only geometry used to calculate the polarizability was the MP2/6-31g(d) optimized D_{3h} configuration. The obtained molecular polarizabilities (three configurations for $EMIM^+$ and one configuration for NO_3^-) were fitted with Thole's smearing atomic polarizability model. The fitted atomic polarizabilities are shown in Figure 1, and the molecular polarizabilities from the ab initio calculations and from the fitted atomic polarizabilities are compared in Table 1. Thole's model with smearing factor $a = 2.392$ accurately fits the ab initio anisotropic polarizabilities for both $EMIM^+$ and NO_3^-.

It should be mentioned that though Thole's model effectively damps the short-range dipole−dipole interactions thereby reducing the likelihood of the singularity problem, dipole divergence may still occur, as observed in our preliminary MD simulation using the above fits. Though dipole divergence is extremely unlikely when using the above fitted atomic polarizabilities and the smearing factor $a = 2.392$, which were used to successfully simulate IL/vacuum interfaces for up to 2 ns,[103] it occurred in a 10 ns MD simulation. Therefore, in this study, we adopted Thole's original smearing factor $a = 2.089$, while using the same atomic polarizabilities listed in Figure 1. A smaller smearing factor enhances screening, thus reducing ionic polarizabilities by 7−8% of the original values, which are listed in Table 1. MD simulation with the polarizable model was stable for more than 10 ns using Thole's original smearing factor. Further work will address accurately fitting ionic polarizability while maintaining stable MD trajectories.

TABLE 1: The Ab Initio Molecular Polarizabilities and the Fits by Thole's Model

molecular	configuration	method	α_1^e	α_2^e	α_3^e	$\bar{\alpha}^f$
$EMIM^+$	Min[a]	ab initio[b]	8.68	11.70	14.88	11.75
		fit[c]	8.60	11.89	14.66	11.71
		Thole[d]	8.28	10.93	13.06	10.76
	cis	ab initio[b]	8.26	12.23	14.69	11.72
		fit[c]	8.11	12.49	14.58	11.73
		Thole[d]	7.90	11.41	13.02	10.77
	trans	ab initio[b]	8.25	11.82	15.16	11.74
		fit[c]	8.11	11.97	15.22	11.76
		Thole[d]	7.90	11.00	13.49	10.80
NO_3^-	D_{3h}[a]	ab initio[b]	3.03	5.78	5.78	4.86
		fit[c]	3.03	5.77	5.77	4.86
		Thole[d]	3.23	5.13	5.13	4.50

[a] The MP2/6-31 g(d) optimized structure, as shown in Figure 1. [b] Ab initio ionic polarizabilities were calculated with the MP2/aug-cc-pVDZ level of theory. [c] The fitted atomic polarizabilities are listed in Figure 1 and the Thole smearing factor is $a = 2.392$. [d] Ionic polarizabilities with the atomic polarizabilities listed in Figure 1 and the Thole smearing factor $a = 2.089$, which is used in MD simulation (see text). [e] α_1, α_2, and α_3 give the three components of the molecular polarizability along the principal axes. [f] $\bar{\alpha} = \mathrm{Tr}\langle\alpha\rangle/3$ gives the isotropic molecular polarizability.

II.2. Fitting Point Partial Charges. The electrostatic potential (ESP) of $EMIM^+$ was calculated at MP2/6-31g* for the three configurations mentioned above. The ESPs for those configurations were then fitted simultaneously with the RESP method[104] to obtain the point partial charges for $EMIM^+$. The point partial charges of NO_3^- were obtained by fitting the ESP of the D_{3h} minimum energy configuration. The fitted partial charges are also shown in Figure 1.

This completes the procedure for fitting point partial charges, which is the same for both the nonpolarizable model and the polarizable model. For an isolated ion in gas phase without external electric fields, as in the ESP calculation, the induced dipole $\boldsymbol{\mu}_{\mathrm{mol}}$ is defined to be zero in this study, and the charge cloud is only represented by the point partial charges. $\boldsymbol{\mu}_{\mathrm{mol}}$ is induced only when external electric fields or reaction fields generated by other ions are switched on, resembling Applequist's derivation of the interactive dipole model[97] in eqs 5 and 6. Therefore, in the current study, the intramolecular charge−dipole interactions are completely ignored, that is, there is no "self-induced dipole" in the absence of external electric fields. As a consequence, for an isolated molecule without external fields, the nonpolarizable model and the polarizable model are equivalent. Once the external electric field is switched on, for example, by the electrostatic interactions among ions in the IL system, the polarizable model better represents the deformation of the charge cloud of the ions. In contrast, all of the intramolecular dipole−dipole interactions are necessary for rebuilding the anisotropic molecular dipole from the isotropic atomic dipoles.

II.3. Forcefields for the Nonpolarizable and Polarizable Models. The forcefield for the nonpolarizable model takes the standard form, such as

$$V_{\text{nonpolarizable}} = \sum_{\text{bonds}} k_b(r - r_0)^2 + \sum_{\text{angles}} k_\theta(\theta - \theta_0)^2 + \sum_{\text{dihedrals}} V_n[1 - \cos(n\phi - \gamma)] + \sum_i \sum_{j>i} \left\{ 4\varepsilon_{ij}\left[\left(\frac{\sigma_{ij}}{r_{ij}}\right)^{12} - \left(\frac{\sigma_{ij}}{r_{ij}}\right)^{6}\right] + \frac{q_i q_j}{r_{ij}} \right\} \quad (7)$$

The forcefield parameters for the $EMIM^+/NO_3^-$ IL are given in our previous studies.[25,63] The forcefield for the polarizable model is given by

$$V_{\text{polarizable}e} = V_{\text{nonpolarizable}} - \sum_i \boldsymbol{\mu}_i \cdot \boldsymbol{E}_i - \sum_i \sum_{j>i} \boldsymbol{\mu}_i \boldsymbol{\mu}_j : \boldsymbol{T}_{ij} + \sum_i \frac{\boldsymbol{\mu}_i \cdot \boldsymbol{\mu}_i}{2\alpha_i^2} \quad (8)$$

where the first term is given by eq 7, the second term represents charge−dipole interactions, the third term represents dipole−dipole interactions, and the last term is the energy required to induce the dipole. In eq 8, $\boldsymbol{E}_i = \sum_{j\neq i} q_j \boldsymbol{E}_{ij}^{\text{f}}$, in which $\boldsymbol{E}_{ij}^{\text{f}}$, given by eq 3, is the fractional electric field on atom i generated by the partial charges of all other atoms except the intramolecular atoms within the same ion, $\boldsymbol{T}_{ij}$ is the dipole field tensor given in eq 4, and the induced atomic dipole $\boldsymbol{\mu}_i$ and $\boldsymbol{\mu}_j$ are given by eq 5, respectively. It should be mentioned that in the above expression, all the charge−dipole and dipole−dipole interactions are subjected to Thole smearing attenuation, which is not the same as in our previous studies[34,63,103,105] in which only intramolecular dipole−dipole interactions within bond, angle, and dihedral terms are subjected to Thole smearing.

The polarizable forcefield with the interactive atomic dipole model was implemented in the DL_POLY MD simulation package[106] and parallelized with the replicated data method.[107] The induced dipoles were calculated either by the iterative method or by the ext-L method (see Appendix). The implementation of the above polarizable forcefield for an infinite periodic system with the Ewald summation for the long-range electrostatic interactions has been well formulized in the literature.[108,109]

II.4. Simulation Details. Two parallel simulations of the $EMIM^+/NO_3^-$ IL system with the polarizable model and the nonpolarizable model, respectively, were performed. The forcefield parameters for the nonpolarizable model were taken from the AMBER forcefield,[110] as described previously.[25,63] The polarizable model takes all forcefield parameters as well as partial charges from the nonpolarizable model. In addition, an isotropic polarizability is assigned to each atom site (cf. Figure 1). For both models, the IL system consists of 400 $EMIM^+/NO_3^-$ ion pairs (9200 atoms) with an all-atom, all-flexible representation. The densities, determined by constant NPT MD simulations[111] for 2 ns with $P = 1$ atm and $T = 400$ K, were 1.182 g/cm^3 for the polarizable model and 1.181 g/cm^3 for the nonpolarizable model. For comparison, the experimental density for the crystal state of $EMIM^+/NO_3^-$ is 1.279 g/cm.[310] Equilibrium NVT runs were then performed for another 1 ns, with the system coupled to a Nosé-Hoover thermostat[112,113] at $T =$ 400 K. The production runs were performed with constant NVE simulation.[108,109] Periodic boundary conditions (PBC) were employed with a cubic simulation cell. Long-range charge−charge, charge−dipole, and dipole−dipole interactions were handled by Ewald summation, with eight **k** vectors along each dimension in reciprocal space. For the polarizable model, the ext-L method (see Appendix) was used for the dipole degrees of freedom. The integration time step was 0.4 fs for the polarizable model and 1.0 fs for the nonpolarizable model. The simulations for both models were run for 10 ns, with the phase space data (velocities, coordinates, and the induced dipoles for the polarizable model) sampled every 4 fs.

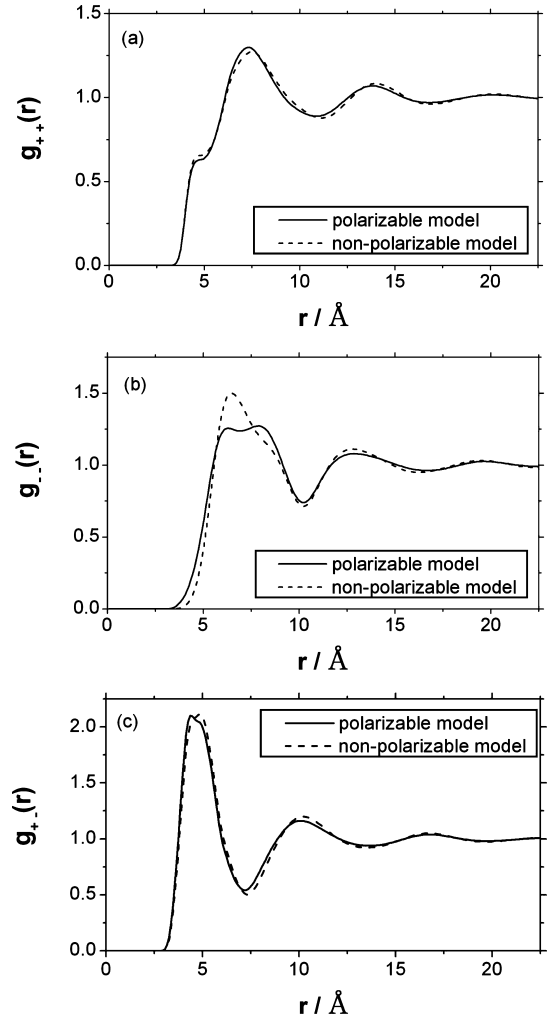

Figure 2. The center-of-mass partial radial distribution functions of (a) cation−cation, (b) anion−anion, (c) cation−anion. The black line is for the polarizable model and the dashed line is for the nonpolarizable model.

To measure the effectiveness of the charge screening within ILs, we set up another four simulations by inserting a nonpolarizable bare ion (of charge +1e and −1e) into both the polarizable IL model and the nonpolarizable IL model constructed above. The probe ion ($\varepsilon = 0.24$ kcal/mol and $\sigma = 3.49$ Å) is the same as that was adopted by Lynden-Bell.[114,115] The simulations with probe ion were run for 2 ns with phase space data sampled every 20 fs.

III. Structural Properties

III.1. Radial Distribution Functions and Structure Factors for Ions. The center-of-mass partial radial distribution functions (PRDFs) of cation−cation $g_{++}(r)$, anion−anion $g_{--}(r)$, and cation−anion $g_{+-}(r)$ are shown in Figure 2. A distinct feature in this figure is that both the polarizable model and the nonpolarizable model exhibit very long-range spatial correla-

tions, and the oscillations in the PRDFs extend up to 23 Å, which is about half the length of the simulation box. On the other hand, the short-range correlations are relatively weak compared to the inorganic molten salt.[116] As can be seen in Figure 2, the maxima and minima are not far from the reduced average number density of unity, especially $g_{++}(r)$ and $g_{--}(r)$, for which the ions carry the same type of charges. The first maximum of $g_{++}(r)$ is much broader and weaker than that of $g_{+-}(r)$, in agreement with experimental measurements of a slightly different system, $DMIM^+/Cl^-$.[4] This is expected because the IL ions are quite bulky. As a result, the first coordination shells for cation−cation and anion−anion are well beyond 10 Å, and that for cation−anion is above 7 Å. Comparing PRDFs between the polarizable and the nonpolarizable models, it can be seen that for the polarizable model the first maxima of the PRDFs shift to a shorter distance, which demonstrates that the ions are in closer contact. When electronic polarization is present, an additional screening effect reduces the Coulombic repulsion between like ions and the cation−anion attraction. Integrating up to the first coordination shell gives coordination numbers of seven, six, and five for $g_{++}(r)$, $g_{--}(r)$, and $g_{+-}(r)$, respectively.

The structural properties were also characterized by the partial center-of-mass static structure factor, which is given by

$$S_{\alpha\beta}(k) = \langle \rho_\alpha(\mathbf{k})\rho_\beta(-\mathbf{k})\rangle \tag{9}$$

where $\rho_\alpha(\mathbf{k}) = \sum_{i=1}^{N_\alpha} \exp(-i\mathbf{k}\mathbf{r}^c_{\alpha,i})$ is the spatial Fourier component of the number density for ion type α. The angular brackets average over all wave-vectors of the same magnitude. The structure factors are plotted in Figure 3. The simulation results are comparable to the experimental[5] and simulation[62] studies of a slightly different ionic liquid 1,3-dimethylimidazolium hexafluorophosphase ($DMIM^+/PF_6^-$). $S_{++}(k)$ and $S_{+-}(k)$ are similar for both models. For the polarizable model, the principal peaks of $S_{++}(k)$ and $S_{--}(k)$ and the first minimum of $S_{+-}(k)$ are less sharp, and less oscillations occur over the entire range of wave vectors, indicating that the polarizable model is less structured. Although both the polarizable and nonpolarizable models were simulated at the same temperature, the effect of using a polarizable model is similar to running the nonpolarizable model at a higher temperature.[90] The most significant difference between the two models is seen in $S_{--}(k)$, analogous to the difference in $g_{--}(r)$. The shift of the principal peak toward lower wave-vectors indicates a larger closest anion−anion pair separation for the polarizable model. However, the shift of the third peak to higher wave vectors indicates more screening of the Coulombic repulsion caused by the induced dipoles, bringing the anions in closer contact for the polarizable model. In the intermediate range, that is, for wave vectors between 0.2−0.9 $Å^{-1}$, the amplitude of $S_{--}(k)$ for the polarizable model is consistently larger than that for the nonpolarizable model, indicating that the NO_3^- ions are more strongly correlated for the polarizable model than for the nonpolarizable model in this range. However, at $T = 400$ K, the overall intermediate range order (IRO) is weak for both models. Considering the fact that the simulations were performed at a temperature 89 K higher than the melting point $T = 311$ K of $EMIM^+/NO_3^-$, the IRO effect, if it exists, is significantly reduced. For both models, the packing of cations and anions is largely determined by charge ordering,[94] similar to the study by Ribeiro et al.[117]

III.2. Iso-Density Probability Distributions. A big difference between the polarizable model and the nonpolarizable model is seen in $g_{--}(r)$, as shown in Figure 2b. Since the polarizability of NO_3^- is much smaller than that of $EMIM^+$ (Table 1), and the charge screening due to induction is expected to be weak for NO_3^-, it is somehow surprising to observe such large differences in $g_{--}(r)$. To help explain this further, iso-density probability distributions will be discussed.

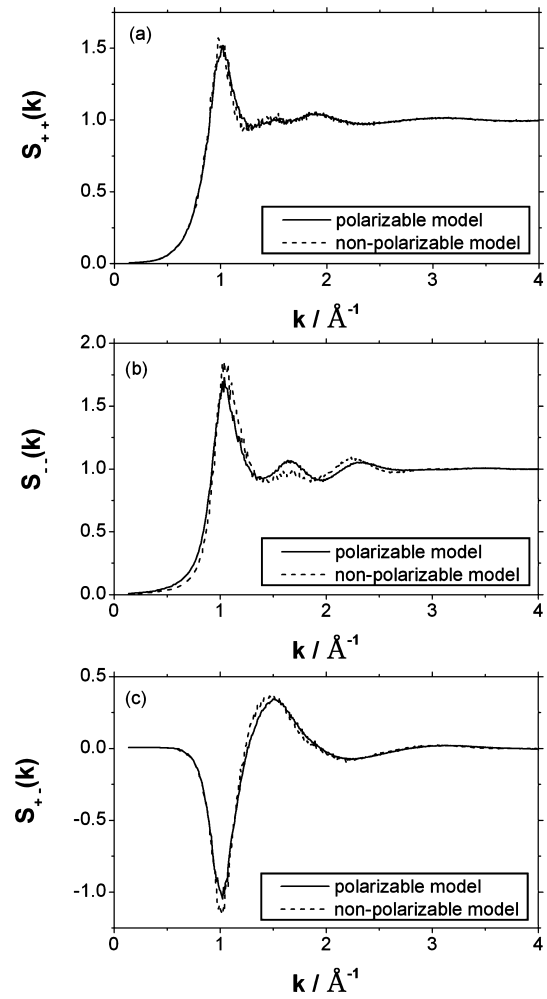

Figure 3. The center-of-mass partial static structure factors for (a) cation−cation, (b) anion−anion, (c) cation−anion, respectively. The black line is for the polarizable model and the dashed line is for the nonpolarizable model.

Figure 4 shows 3D iso-density plots, which demonstrate the anisotropic probability distributions of $EMIM^+$ (yellow) and NO_3^- (iceblue) centered at NO_3^- for both the polarizable model and the nonpolarizable model. The features in Figure 4(a) and (b) can be connected to the two maxima of $g_{--}(r)$ for the polarizable model shown in Figure 2. The two peaks correspond to high density in a shorter distance around the N−O−N edge region and in a longer distance around the O-atom vertex, respectively. Figure 4c,d can be associated with the first maximum in $g_{--}(r)$ of the nonpolarizable model at 6.5 Å. The packing of the NO_3^- ions on a center NO_3^- is correlated with the inner packing of $EMIM^+$ around NO_3^-. For both the polarizable model and the nonpolarizable model, $EMIM^+$ is most likely to pack around the N−O−N edge region. As for the most favorable packing of NO_3^- ions on a center NO_3^-, these two models show rather different patterns. For the nonpolarizable model, NO_3^- ions tend to pack on the edge of the $EMIM^+-NO_3^--EMIM^+$ region, as shown in Figure 4c,d. In contrast, such a pattern is much weaker for the polarizable model, which gives two lower maxima in $g_{--}(r)$ than the single higher maximum in $g_{--}(r)$ for the nonpolarizable model. This

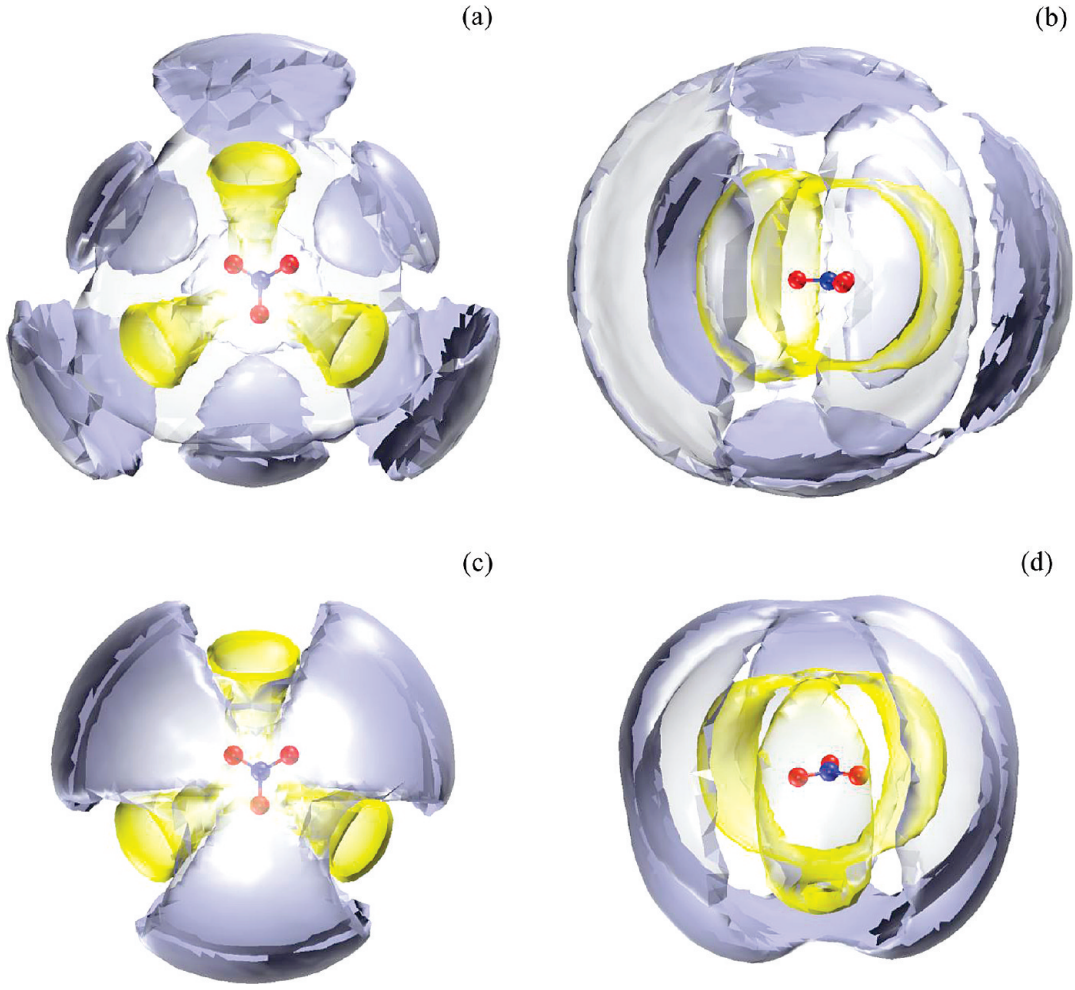

Figure 4. Three-dimensional configuration probability distributions of $EMIM^+$ (yellow) and NO_3^- (iceblue) centered at NO_3^-. (a) Top view and (b) side view of the polarizable model with $\rho_+(x,y,z) = 0.010/Å^3$ and $\rho_-(x,y,z) = 0.0055/Å^3$; (c) top view and (d) side view of the nonpolarizable model with $\rho_+(x,y,z) = 0.010/Å^3$ and $\rho_-(x,y,z) = 0.006/Å^3$. The average number density is $\bar{\rho} = 0.004/Å^3$ for both models.

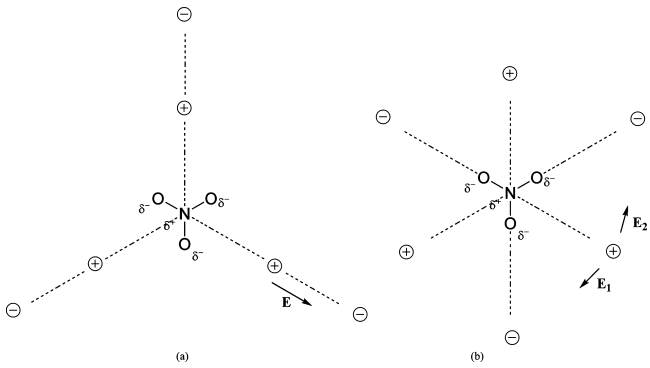

Figure 5. Schematic plots of the projections of the most probable occurrence of other cations and anions on the center NO_3^- plane. (a) Polarizable model; (b) nonpolarizable model. ⊕, cation and ⊖, anion.

feature is quantified in the PRDF plots shown in Figure 2b, that is, $g_{--}(r)$ of the polarizable model has its peak region "cut" compared with that of the nonpolarizable model.

The projection of the most probable occurrence of cations and anions around a center NO_3^- plane is schematically drawn in Figure 5. The packing of the closest cations around the center NO_3^- is basically governed by electrostatic interactions and shows very similar patterns for the polarizable and nonpolarizable models, as also seen in Figure 4. Meanwhile, the packing of the closest NO_3^- around the center NO_3^- shown in Figure 5a tends to have a stronger local electric field **E** on the closest $EMIM^+$. However, in the most probable anion−cation−anion packing pattern for the nonpolarizable model shown in Figure 5(b), the local electric fields $\mathbf{E}_1$ and $\mathbf{E}_2$ on the closest $EMIM^+$, due to the closest anions, tend to cancel each other. Since $EMIM^+$ is much more polarizable than NO_3^-, a stronger local electric field on $EMIM^+$ enlarges the induced dipole on it, which is energetically favorable. The trade-off for the decrease in system energy caused by the polarization effect is the increase of Coulombic energy since the packing shown in Figure 5a is not as favorable for the Coulombic interaction as that shown in Figure 5b. Thus, the rather different $g_{--}(r)$ for the polarizable and nonpolarizable models may be explained by the polarization effect on the cations. The cations have much larger polarizability than the anions, so the anions rearrange themselves in favor of the electric induction effect on the cations. This is in agreement with the study of molten $ZnCl_2$. In both cases, the less polarizable ions rearrange themselves to maximize the local electrical field on the more polarizable ions.[86]

It should be emphasized that the above discussion on the polarization effect may oversimplify the situation because the IL system is quite complicated and Figure 5 does not take into account the anisotropic spatial arrangement of the ions. Further study on the polarization effect is therefore necessary. Although neutron scattering experiments have probed the structural properties of ILs,[4,5] $g_{--}(r)$ has not yet been reported, probably

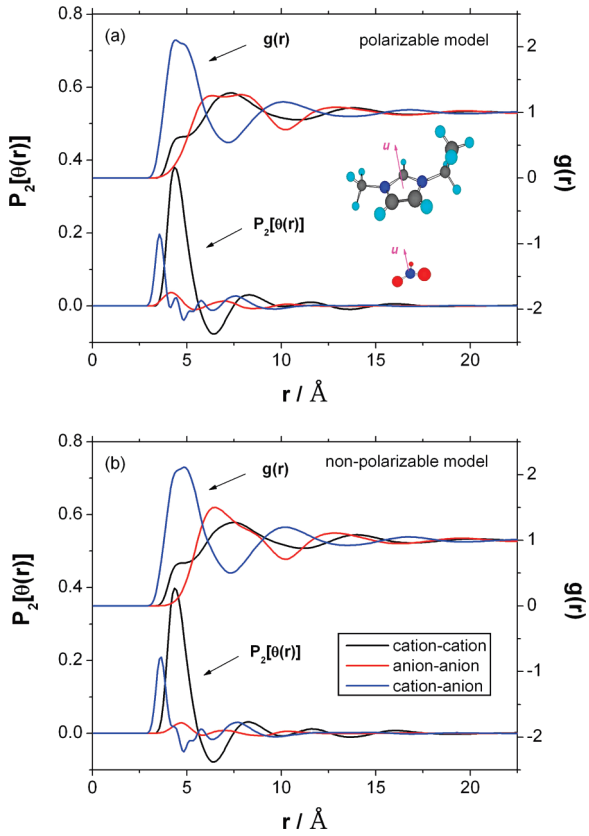

Figure 6. The static orientational ordering parameter for (a) the polarizable model and (b) the nonpolarizable model. For better illustration, the center-of-mass partial radial distribution functions in Figure 2 are also reproduced in this figure. The same legend and definition of the **u** vectors (direction normal to the imidazolium ring or NO_3^- plane) are used for both models.

because neutron scattering mainly probes hydrogen atoms in the system and is insensitive to the anion−anion spatial correlation. A recent study of the same system with charge response kernel (CRK) model by Sato et al. also found broad first peak in $g_{--}(r)$.[118] Even though a polarizable model should more appropriately and accurately represent structural properties, further validation by experiments is desired to verify this.

III.3. Orientational Ordering. It is of interest to note that the small "bump" at ~4.4 Å in $g_{++}(r)$ for both the polarizable and nonpolarizable models was also observed in the experimental study on $DMIM^+/Cl^-$,[4,5] in which the small bump in $g_{++}(r)$ occurs at about 4 Å; the small difference in the bump position may result from the smaller size of $DMIM^+$ compared to $EMIM^+$. Figure 6 shows the static orientational ordering of cation−cation, anion−anion, and cation−anion for both the polarizable and nonpolarizable models according to the following expression

$$P_2[\theta(r)] = \frac{1}{2}\langle 3\cos^2\theta(r) - 1\rangle = \frac{1}{2}\langle 3[\mathbf{u}(r)\cdot\mathbf{u}(0)]^2 - 1\rangle \quad (10)$$

where $\mathbf{u}(r)$ is defined as the unit vector perpendicular to the ionic plane, as shown in Figure 6. For better illustration, the PRDFs from Figure 2 are reproduced in Figure 6. A distinct feature is the strong peak in the cation−cation $P_2[\theta(r)]$ at the position where the "bump" in $g_{++}(r)$ occurs. The peak values for the cation−cation orientational order correspond to ~41° and ~39° for the polarizable and nonpolarizable models, respectively.

The experimental crystal structure of $EMIM^+/NO_3^-$ shows that the stacking of the ions is nearly parallel with the interplane separation of the ions at 4.5 Å.[10] Therefore, the "bump" observed in $g_{++}(r)$ may be explained by this crystal structure feature, which the system seems to "remember" even at a much higher temperature than the melting point of 311 K. This feature is also seen in the anion−anion $P_2[\theta(r)]$ in Figure 6. Since NO_3^- is smaller and thus has larger thermal fluctuations than $EMIM^+$, the above crystal structure feature does not result in a strong signal in either $P_2[\theta(r)]$ or $g_{--}(r)$. In a wide-angle X-ray scattering (WAXS) spectroscopy study at room temperature on $BMIM^+/I^-$,[119] the short-range liquid structure was found to reflect its crystal structure, that is, a sharp peak at 4.4 Å in the electronic density distribution. Since I^- has many more electrons than H, N, and C atoms, WAXS mainly probes the iodine−iodine spatial correlations. An AIMD simulation study of $DMIM^+/Cl^-$ also found that the peak at 4.1 Å in $g_{++}(r)$ is a result of the parallel arrangement of the $DMIM^+$ planes, which suggests $\pi-\pi$ interactions between the imidazolium rings.[59] Imidazolium ring stacking has also been studied in MD simulations with nonpolarizable forcefields.[22,57]

In order to calibrate the more detailed orientational ordering, Figure 7 shows the 2D distribution functions $g(r,\alpha)$ and $g(r,\text{offset})$, both of which are for the distance r between the geometrical centers of neighboring imidazolium rings as well as either the angle α between imidazolium ring normals, for the former, or the imidazolium ring offset distance, for the latter, cf. inset of Figure 7a. The overall trend for short-range orientational ordering is very similar for both the polarizable and nonpolarizable models. $g(r,\alpha)$ peaks at (4.05 Å, 19.7°) and (4.1 Å, 22.2°), respectively, for the polarizable and nonpolarizable models, while $g(r,\text{offset})$ peaks at (4.05, 2.0 Å) (4.10, 1.95 Å) for both models. Therefore, $EMIM^+$ cations pack nearly parallel to each other at short distances. The ring center distances and offsets are in good agreement with previous simulations of slightly different imidazolium-based ILs.[22] However, comparing with previous simulations of $BMIM^+/NO_3^-$, the distance r for the peak position of $g(r,\alpha)$ in this study is larger than the 3.7 Å distance reported by Soares and co-workers.[57] This may be attributed to the reduced van der Waals (VDW) interaction used in Soares' study. Since electrostatic interactions dominate in this system, the parallel alignment of the imidazolium rings in the local packing may be attributed to the hydrogen bonds.[22]

III.4. Atomic Radial Distribution Functions and Hydrogen Bonding Networks. Figure 8 shows the site−site PRDFs for the H-atoms and C-atoms of $EMIM^+$ with respect to the O-atoms of NO_3^- for both the polarizable and nonpolarizable models. The PRDFs are normalized to unity at long distance for better comparison. O-atoms are most likely to contact the H2 atom (cf. Figure 1) of the imidazolium ring, followed by the H4 and H5 atoms. The anions show less tendency to contact the H-atoms of the side-chains. Thus, as expected, the H-atoms of the imidazolium ring are better hydrogen bond donors to the anions. Similar results were also found in other MD simulations.[9,22] In addition, the peak of the H2−O PRDF for the polarizable model is much more intense than that for the nonpolarizable model. The peak positions for the H2−O PRDF are at 2.35 and 2.45 Å for the polarizable and nonpolarizable models, respectively. Thus, the anion is more likely to form hydrogen bond with the H2 atom for the polarizable model. On one hand, electronic polarizability brings the atoms into closer contact;

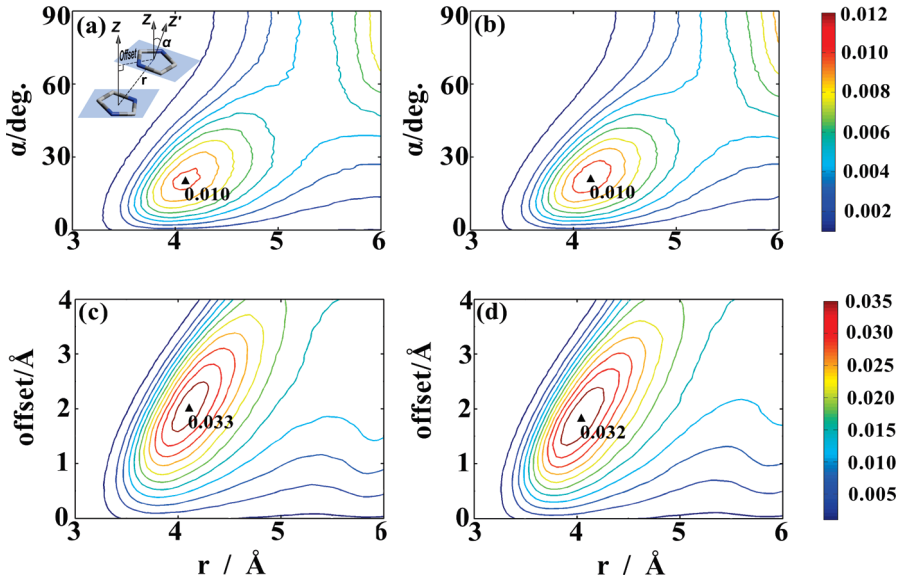

Figure 7. Two dimensional distance, r, between the geometrical centers of the imidazolium rings and angle, α, between imidazolim ring normals for (a) polarizable model and (b) nonpolarizable model. Two-dimensional distance, r, between the geometrical centers of the imidazolium rings and offset distance between the geometrical centers of the imidazolium rings for (c) polarizable model and (d) nonpolarizable model. The geometrical center of imidazolium ring, ring normals (z, z'), and offset are depicted in inset of (a).

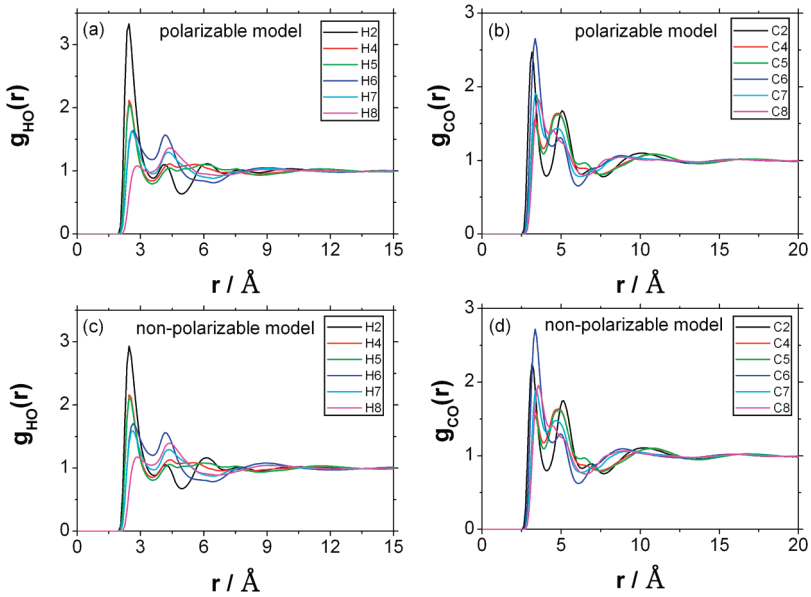

Figure 8. The site−site partial radial distribution functions for the H-atoms and C-atoms of $EMIM^+$ with the O-atoms of NO_3^- for both the polarizable and nonpolarizable models. (a) $g_{HO}(r)$ for the polarizable model, (b) $g_{CO}(r)$ for the polarizable model, (c) $g_{HO}(r)$ for the nonpolarizable model, (d) $g_{CO}(r)$ for the nonpolarizable model. The indices of the H- and C-atoms are shown in Figure 1.

on the other hand, no polarization leads to more pronounced long-range oscillations.

$g_{CO}(r)$ also shows some interesting features. The closest interionic C−O contact involves the C2-atom of the imidazolium ring, in agreement with $g_{HO}(r)$. The peaks of the C2−O PRDFs are at 3.15 Å for both the polarizable and nonpolarizable models, but the peak for the former is more intense. The experimental measurement of crystal $EMIM^+/NO_3^-$ indicates that the closest interionic contact is the C2−O pair distance of 3.078 Å.[10] The ∼0.1 Å difference in peak position between the experimental crystal state and the simulated liquid state may be explained by the higher temperature (400 K) and lower density of the simulation.

Another feature in $g_{CO}(r)$ is that the most intensive peak is seen for the C6−O PRDF for both models. When a NO_3^- forms a hydrogen bond with H2 or H4 on the imidazolium ring, one of the H-atoms on the methyl side-group also usually forms a hydrogen bond with one of the other O-atoms of that NO_3^-. This can also be seen from the H6−O PRDF. It has the largest second maximum, which is almost as intense as the first maximum, with one H6-atom in close contact with the anion and another two H6-atoms far apart. The net result is that the intensity of the C6−O PRDF is correlated with the H2−O and H4−O hydrogen bonds. If there is a close C2−O (H2−O) or C4−O (H4−O) contact, a close C6−O contact also likely exists. Figure 9 shows three snapshots taken randomly from the last frame of a 10 ns MD simulation for the polarizable model. The hydrogen bonds are identified for the NO_3^- anion with the hydrogen atoms H2, H4, and H5 on the imidazolium ring of $EMIM^+$.

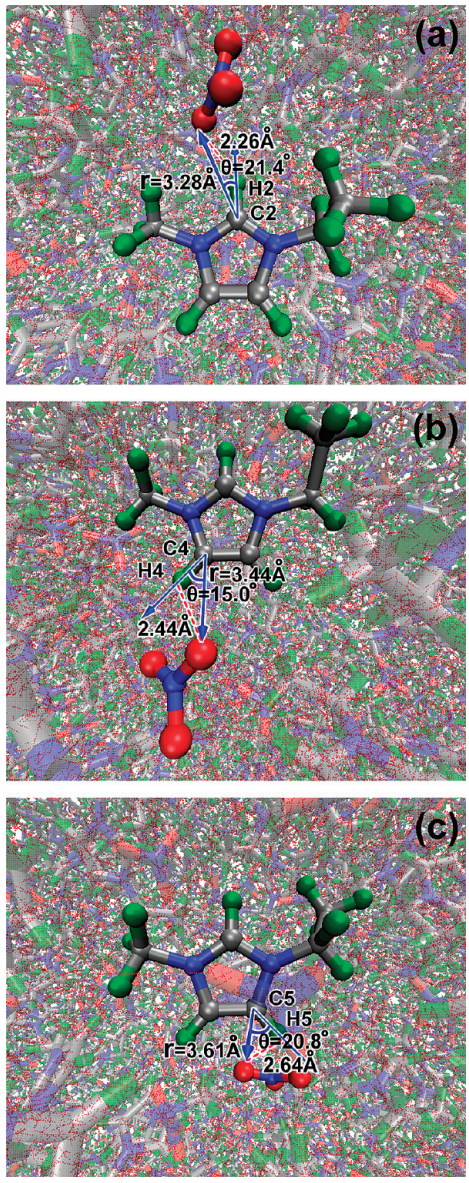

Figure 9. Three snapshots of hydrogen bonding between NO_3^- and H2 (a), H4 (b), and H5 (c) atoms on the imidazolium ring of $EMIM^+$. The snapshots were taken randomly from the polarizable IL system. Randomly selected $EMIM^+$ and NO_3^- pairs that hydrogen bond are shown as ball-stick models, while other cations and anions are also shown subtransparently. r represents O−C distance and θ represents O−C−H angle. The red dashed lines highlight the hydrogen bonding network.

Figure 10 shows the two-dimensional O−C distance and O−C−H angle distribution in which the hydrogen atoms are H2, H4, and H5 on the imidazolium ring as in Figure 10 for both models. Though there are three oxygen atoms on NO_3^-, only the shortest O−C distance is identified and plotted in Figure 10. It can be seen that the polarizable effect brings the ions into closer contact. Specifically, the peaks occur at (3.20 Å, 38.4°), (3.40 Å, 27.8°), and (3.40 Å, 27.3°) between the oxygen atoms of NO_3^- and C2, C4, and C5 atoms of $EMIM^+$, respectively, for the polarizable model, and the peaks occur at (3.20 Å, 39.9°), (3.40 Å, 28.8°), and (3.40 Å, 28.3°), respectively, for the nonpolarizable model. The peak intensity of O−C2 is much stronger than O−C4 and O−C5, indicating the stronger hydrogen bond donating ability of H2 on the imidazolium ring. Also, the intensity of the O−C2 peak for the polarizable model is slightly higher than that of the nonpolarizable model, while the intensity of the O−C5 peak is weaker for the former, consistent with Figure 8. Thus, hydrogen bonds form easier in the polarizable rather than in the nonpolarizable model. The weak peaks at (4.85 Å, 41.0°) and (4.90 Å, 43.5°) in Figure 10a,b highlight the longer-range ordering of the hydrogen bonding network. The contacted, but not hydrogen-bonded, IL ions exhibit long-range correlation, which may also contribute to the extended PRDF in Figure 2. Therefore, the condensed-phase properties of ILs are strongly influenced by hydrogen bonding.

Figure 11 shows the global minima of two $EMIM^+/NO_3^-$ isolated ion pairs for the polarizable and nonpolarizable models, as well as the optimized (B3LYP/aug-cc-pVDZ) structure with ab intio calculations. The global minima for the clusters, for the polarizable and nonpolarizable models, were calculated by the parallel-tempering basin hopping algorithm,[120] which was coded in a modified version of the DL_POLY package,[106] with the same classical force field used in MD simulation. The ab initio optimization was performed with Gaussian03,[102] with the initial structure taken from Figure 11a, and thus may or may not be the global minimum. The classical forcefield optimized structures are in reasonable qualitative agreement with the B3LYP/aug-cc-pVDZ optimized structure, though not in quantitative agreement. Several distances and angles, characterizing hydrogen bonding and ion packing, are shown in Figure 11. This figure may be related to the ion packing shown in Figure 7 and hydrogen bonding shown in Figure 10, though the latter is a statistical ensemble average over a 10 ns simulation of bulk liquid. The optimized ion pairs clearly demonstrate parallel imidazolium ring packing, bridged by hydrogen bonds between $EMIM^+$ and NO_3^-. Comparing the optimized structures of the polarizable and nonpolarizable models, the O−C and O−H distances are slightly shorter for the former. Thus, the additional charge−dipole and dipole−dipole interactions introduced by the polarizable model bring ions in close contact in the short range. In addition, the interplane distances are 4.28, 4.27, and 4.15 Å for the polarizable model, the nonpolarizable model, and B3LYP/aug-cc-pVDZ, respectively. These interplane distances are slightly larger than the typical $\pi-\pi$ stacking interplane distance (3.2 Å) and offset (1.4 Å) reported by Gordon and co-workers for the triazolium-based ILs.[55] Thus, the parallel packing of imidazolium rings may be attributed to hydrogen bonding, as shown in Figure 11 and as discussed by Holm and co-workers.[22] The distance between the C2 atom of $EMIM^+$ and the oxygen atom, which is hydrogen bonded to the C2 atom of the other $EMIM^+$, is 4.58 and 4.70 Å, respectively, for the polarizable and nonpolarizable models. Such spatial correlation may be related to the weak peaks at 4.85 and 4.90 Å in Figure 11a,b.

III.5. Tail Aggregation and Spatial Heterogeneity. Although spatial heterogeneity is very weak in IL systems with very short alkyl side-chains, it has been shown that tail aggregation is still detectable for $EMIM^+/NO_3^-$ from MD simulation,[37] though such effect is difficult to probe experimentally.[45] Thus, the influence of the polarization effect on spatial heterogeneity can be checked for this IL system. Spatial heterogeneity in ILs can be characterized using the PRDF between the terminal carbon atoms on the alkyl side-chains. Figure 12 shows the PRDFs for C8−C8 with both the polarizable and nonpolarizable models. The first-peak height of the polarizable model is clearly higher than that of the nonpolarizable model, indicating that polarization enhances tail aggregation.

In order to quantify this, a heterogeneity order parameter (HOP)[31,37] for a site "i" is defined as

$$h_i = \sum_j \exp(-r_{ij}^2/2\sigma^2) \qquad (11)$$

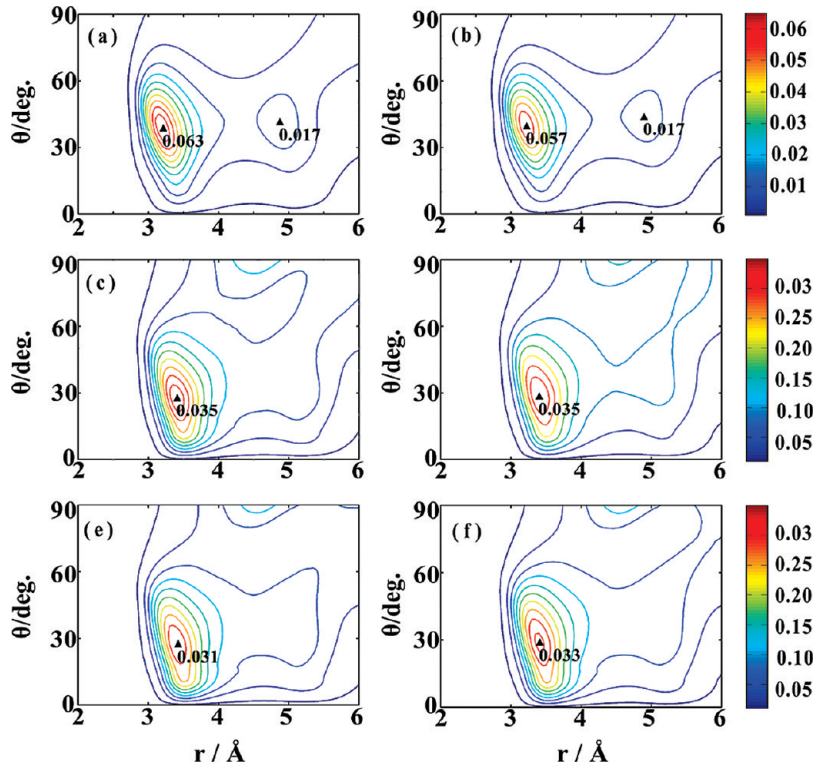

Figure 10. The 2D shortest O−C distance (r) and O−C−H angle (θ) distribution, in which the O-atom is on the NO_3^- anion and the C- and H-atoms are the C2, C4, C5, and H2, H4, H5 (cf. Figure 1), respectively on the imidazolium ring of the $EMIM^+$ cation; O−C2−H2, O−C4−H4, and O−C5−H5 are depicted in (a,c,e) for the polarizable model, and in (b,d,f) for the nonpolarizable model.

where r_{ij} is the length of the vector $\boldsymbol{r}_i - \boldsymbol{r}_j$ under periodic boundary conditions and $\sigma = L/N^{1/3}$ with L being the side length of the cubic simulation box and N as the total number of sites.

The average HOP is computed by averaging over all N_s sites of interest such that

$$h = \frac{1}{N_s}\sum_{i=1}^{N_s} h_i \tag{12}$$

For a given N_s total number of sites, a larger HOP demonstrates stronger spatial heterogeneity. The HOPs calculated for the C8 atoms in $EMIM^+/NO_3^-$ with both the polarizable and nonpolarizable models are 15.9393 and 15.9331, respectively. In agreement with Figure 12, the polarizable model shows a stronger spatial heterogeneity than the nonpolarizable model. The HOPs were also calculated for the headgroup (center of mass of the imidazole ring) and the anion (center of mass of NO_3^-) and are listed in Table 2. Although the average values of the HOPs with the polarizable model are slightly larger than those with the nonpolarizable model, the difference is within statistical error. This indicates that, while the polarization effect significantly changes the local structure of the charged groups, as illustrated in Figure 6, it has much less influence on their global distribution.

According to the results shown in Figure 12 and Table 2, it can be concluded that, although spatial heterogeneity for ILs is observed in both the polarizable and nonpolarizable models, polarizability makes a quantitative difference at short-range. The enhancement of spatial heterogeneity due to the polarization effect may possibly be explained by stronger intermolecular electrostatic interactions among the cations and anions. As a consequence of polarization, the nonpolar ethyl side groups are more "pushed" away by the polar groups and aggregate more. The lower entropy associated with the more aggregated state may be balanced by lower enthalpy, and this hydrophobic-like interaction may be of interest to explore in further studies. Thus, side-chain van der Waals interactions do not significantly determine the spatial heterogeneity in short-chain ILs. Polarization enhances spatial heterogeneity more for longer alkyl side-chain ILs, as evidenced from the polarizable[37] and nonpolarizable[121] results for $OMIM^+/NO_3^-$.

III.6. Charge Screening. In this section, we measure the charge screening effectiveness by inserting a nonpolarizable bare ion (of charge +1e and −1e) into the IL bulks of both the polarizable and the nonpolarizable models. The potential $\varphi(r)$ due to IL solvent at distance r to the probe ion may be written as[114,115]

$$\varphi_c(r) = -\int_0^r \mathrm{d}r' \frac{1}{r'^2}\int_0^{r'} \mathrm{d}r\, 4\pi r^2 \rho_c(r) = \varphi_c(0) + \frac{1}{r}\int_0^r 4\pi r'^2 \rho_c(r')\mathrm{d}r' - \int_0^r 4\pi r' \rho_c(r')\mathrm{d}r' \tag{13}$$

in which $\varphi_c(0) = \langle \sum_{j\neq i} q_j/r_{ji} \rangle$ is the averaged potential of charge j on the probe ion i, and $\rho_q(r)$ is the spherically radial charge density around the probe ion. The total potential at distance r from the probe ion, contributed from both the solvent and the probe ion via the permanent charges, is

$$\varphi_q(r) = \frac{1}{4\pi\varepsilon_0}\left(\varphi_c(r) + \frac{q_i}{r}\right) \tag{14}$$

in which $\varphi_i(r) = q_i/4\pi\varepsilon_0 r$ is the potential for the bare probe ion i.

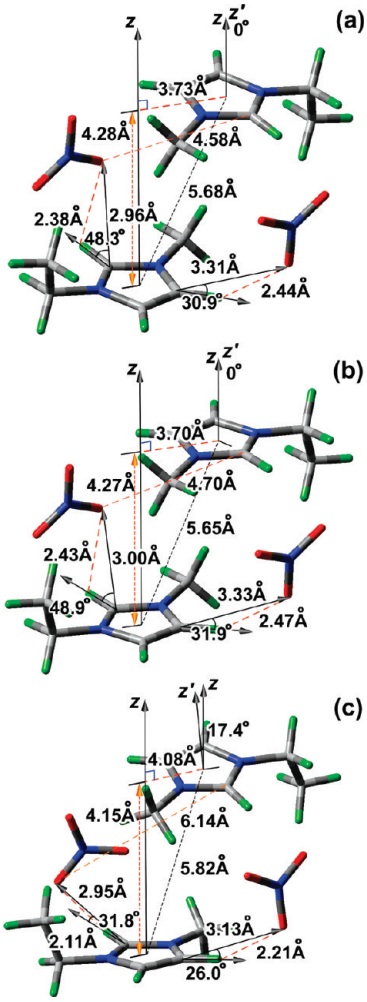

Figure 11. The optimized minimum energy structure of two $EMIM^+/NO_3^-$ ion pairs for (a) polarizable model, (b) nonpolarizable model, and (c) B3LYP/aug-cc-pVDZ. Some distances and angles characterizing the ion packing and hydrogen bonding structure are listed, and z and z' represent imidazolium ring normals of the two $EMIM^+$.

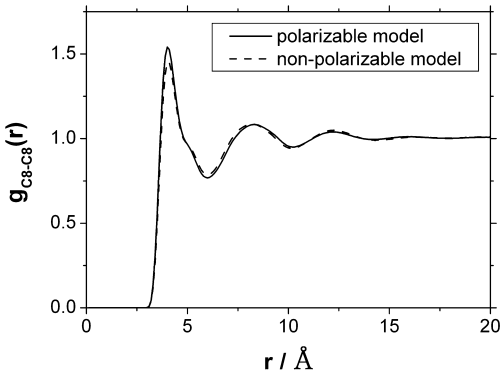

Figure 12. The partial radial distribution function between the terminal carbon atoms on the ethyl side-chains with both the polarizable (solid line) and nonpolarizable (dashed line) models.

For the polarizable model, there is additional screening contributed from induced dipole, and the potential at distance r from the probe ion, contributed by the induced polarization, is

$$\varphi_\mu(r) = \varphi_\mu(0) + \frac{1}{\varepsilon_0}\int_0^r \rho_\mu(r')\mathrm{d}r' \qquad (15)$$

in which $\varphi_\mu(0) = \langle\sum_{j\neq i}\boldsymbol{\mu}_i\cdot\boldsymbol{r}_{ji}/r_{ji}^3\rangle$ is the averaged potential of charge i on the probe ion j, and $\rho_\mu(r)$ denotes the spherically averaged radial dipole density around the probe ion. $\varphi_c(0)$ and $\varphi_\mu(0)$ are calculated by Ewald summation[108,109] during simulation. The total potential of the polarizable model is

$$\varphi_p(r) = \varphi_q(r) + \varphi_\mu(r) \qquad (16)$$

Figure 13 shows the average charge density around the probe ion. For the nonpolarizable model, the charge distribution is contributed by $\rho_c(r)$ only. For the polarizable model, there is additional contribution from the polarization charge density, i.e. $\rho_p = -\nabla\cdot\boldsymbol{P}$, which is calculated by taking the divergence of the $\rho_\mu(r)$ in spherical coordinate numerically. It can be seen that the total charge density around 2.5 Å to the probe ion is stronger for the polarizable model, and the oscillation of the total charge density is weaker for the polarizable model at ca. 5 Å or longer distance to the probe ion, especially for the negatively charged probe ion. For the polarizable model, the polarization charge density $\rho_p(r)$ shows a bimodal distribution between 2 and 4 Å to the probe ion, and it becomes essentially zero at longer distance. The polarization charge by the dipoles enhances total charge density at short distance to the probe ion, while do not alter the charge distribution much at longer distance. It is also of interest to see that the polarization charge distribution appears at shorter distance than the permanent charge distribution, due to the induction of the probe ion. Therefore, the total charge distribution of the polarizable model is quite different from that of the nonpolarizable model.

Figure 14 shows the potential around the negatively and positively charged probe ion, respectively. It can be seen that the probe ion potential is over screened at short-range, that is, shorter than 5 Å to the probe ion. For the polarizable model, the polarization potential caused by the dipoles is quite short ranged, as compared to that by the charge distribution. Furthermore, the polarization potential is correlated with the charge potential, and they work together to stabilize the ion by the electrostatic energy and induction energy. It can be seen that $\varphi_c(r)$ is dominant over all the distance, and $\varphi_\mu(r)$ decays much rapidly to zero at about 5 Å to the probe ion, while the complete screening is achieved at about 10 Å to the probe ion. Comparing the polarizable and the nonpolarizable model, it can be seen that the over screening is stronger for the former at first solvation shell around 2.5 Å to the probe ion, and indicate stronger short-range electrostatic interactions for the polarizable model, indicating a stronger electrostatic interactions for the polarizable model at short-range. Also, because of the charge−dipole interaction, the charge−charge interaction on the probe ion, $\varphi_c(0)$, is reduced for the polarizable model comparing to the nonpolarizable model. On the other hand, the total electrostatic potential at the bare ion, $\varphi_c(0) + \varphi_\mu(0)$, is enhanced for the polarizable model, and this observation is in good agreement with Lynden-Bell's study.[115] The insets of Figure 14 shows the detailed comparison for the total electrostatic potential for the polarizable model, $\varphi_p(r)$, and for the nonpolarizable model, $\varphi_q(r)$. It can be seen that the oscillation of $\varphi_p(r)$ is damped comparing to $\varphi_q(r)$ at long-range, that is, immediately after the first peak or longer distance to the probe ion. Thus, the electrostatic potential of the bare ion is better screened at long-range for the polarizable model, though it shows stronger over screening at short-range.

IV. Summary

In the current study, a second generation polarizable model for the IL $EMIM^+/NO_3^-$, in which both the charge−dipole and

TABLE 2: The Heterogeneity Order Parameters (HOPs)[a] for Tail Groups, Head Groups, and Anions with Both the Polarizable and Nonpolarizable Models

	tail group[b]	head group[c]	anion[d]
polarizable model	15.9393 ± 0.0025	15.7652 ± 0.0002	15.7577 ± 0.0001
nonpolarizable model	15.9331 ± 0.0021	15.7645 ± 0.0003	15.7520 ± 0.0001

[a] Error bars are with 95% confidence interval. [b] C8 atom on the ethyl side chain of $EMIM^+$ (see Figure 1). [c] Geometrical center of imidazolium ring of $EMIM^+$. [d] Center-of-mass of NO_3^-.

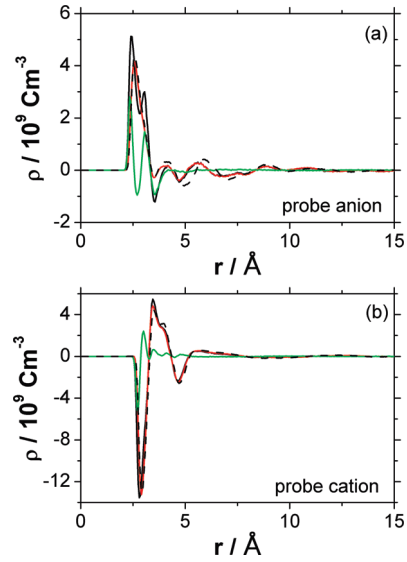

Figure 13. The average charge distribution around a probe ion of charge −1e (a) and +1e (b). Black line is the total charge distribution of the polarizable model, contributed by the permanent charge distribution (red line) and the polarization charge distribution (green line); Black dashed line is the total charge distribution of the nonpolarizable model.

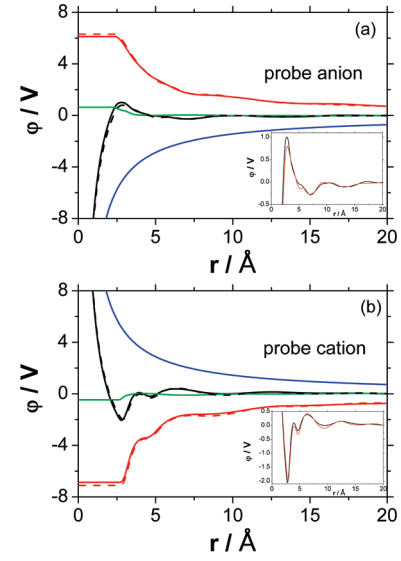

Figure 14. The potential around the probe ion of charge −1e (a) and +1e (b). Black line, total electrostatic potential $\varphi_p(r)$ of the polarizable model; red line, charge potential $\varphi_c(r)$ of the polarizable model; green, polarization potential $\varphi_\mu(r)$ of the polarizable model; black dashed line, total potential $\varphi_q(r)$ of the nonpolarizable model; red dashed line, charge potential $\varphi_c(r)$ of the nonpolarizable model; blue line, potential from the bare probe ion $\varphi_i(r)$. The insets show the detailed comparison for the total electrostatic potential for the polarizable model, $\varphi_p(r)$ (black line) and for the nonpolarizable model, $\varphi_q(r)$ (red line).

dipole−dipole interactions are subjected to Thole smearing,[98,99] was developed. The extended Lagrangian (ext-L) method[87,122] was applied to propagate dipole degrees of freedom and the total system energy was well conserved. Comparisons with the iteration method[99,109,123] for the PRDFs and the distributions of the induced dipole moments were in good agreement.

The current study shows that for both the polarizable and nonpolarizable models this IL retains memory of the crystal structure, even while in a liquid state at a temperature 89 K higher than its melting point. The $EMIM^+$ cations likely pack with neighboring imidazolium rings nearly parallel to each other, bridged by hydrogen bonds with NO_3^- anions. Both models highlight intensive hydrogen bonding with O−H distances slightly closer for the polarizable model due to the additional charge−dipole and dipole−dipole interactions. The oxygen atoms of NO_3^- likely form hydrogen bonds with the hydrogen atoms on the imidazolium ring of $EMIM^+$ with a preference to bond with the H2 atom. The polarizable model has more short-range order due to stronger electrostatic interactions while the nonpolarizable model has more ordered long-range spatial correlation due to less screening. Thus, the polarization effect enhances short-range interactions and reduces long-range interactions, as shown in Figure 13 and 14.

Surprisingly, spatial heterogeneity, due to aggregation of the nonpolar tail groups, is observed in ILs with very short tails, as is the case with $EMIM^+$, though the degree of spatial heterogeneity is small compared to longer side chains.[30,31] Also, such heterogeneity is enhanced by polarization. Since the ethyl tail group is so short, VDW interactions cannot explain such aggregation. On the basis of the weak VDW interactions among the tail groups, we propose that the short-range electrostatic interactions among the polar heads, that is, the imidazolium rings and NO_3^- "push" the nonpolar tails away causing them to aggregate. This interaction may be analogous to the hydrophobic effect. Also, the enhanced short-range electrostatic interactions of the polarizable model lead to even more aggregation. Therefore, aggregation of the nonpolar tails may spontaneously occur even when the attractive part of the VDW interactions among the nonpolar tails is turned off, which might be of interest to future studies. With elongated alkyl side-chains, VDW interactions should become important and compete with the electrostatic interactions.

The anion−anion PRDF in Figure 2b and the anion−cation−anion packing pattern in Figure 5 most significantly distinguish the polarizable model from the nonpolarizable model. We conjecture that the inducement effects of the polarizable model stabilize the anion packing on the vertex of a center anion, as illustrated in Figure 5, causing the apparent difference in the anion−anion PRDF. Such different $g_{--}(r)$ are probably related to a difference in the local electric field. Since $EMIM^+$ possesses higher polarizability, the electric field mainly adjusts NO_3^- position in order to maximize the local electric field around $EMIM^+$. Hopefully, experimental information on ion packing will soon validate these results. The dynamical properties for these two models are reported in the accompanying paper.[100]

Acknowledgment. This study is supported by NFSC (No. 20503013, 20873068) and the 973 Program (2009CB220100) of China. This work cannot be done without the continuous

encourages and supports from Dr. Gregory A. Voth. The authors thank Dr. Christian J. Burnham and Dr. Jonggu Jeon for helpful discussions. The authors are also grateful to Mr. Zhen Cao and Mr. Yuxing Peng for their help on making Figures 7, 9, 10, and 11 for this paper. The allocations of supercomputing time at the Center for High Performance Computing (CHPC) at the University of Utah and Institute of Scientific Computing (NKstars HPC program) at Nankai University are gratefully acknowledged.

Appendix

Comparison of the Iteration Method and the Extended Lagrangian Method for the Induced Dipoles. For the polarizable model, the induced dipole can be calculated either iteratively[99,109,123] or by the extended Lagrangian (ext-L),[87,122] which is expressed as

$$L_{\text{ext}} = T - V = \frac{1}{2}\sum_{i=1}^{3N} m_i \dot{r}^2 + \frac{1}{2}\sum_{i=1}^{3N} m_{\mu,i}\dot{\boldsymbol{\mu}}^2 - V \tag{A1}$$

where $V = V_{\text{polarizable}} = V(\boldsymbol{r}^{3N}) + V(\boldsymbol{\mu}^{3N})$, in which $V(\boldsymbol{r}^{3N}) = V_{\text{nonpolarizable}}$ is defined in eq 7 and $V(\boldsymbol{\mu}^{3N}) = -\sum_i \boldsymbol{\mu}_i \boldsymbol{E}_i^0 - \sum_i \sum_{j>i} \boldsymbol{\mu}_i \boldsymbol{T}_{ij} \boldsymbol{\mu}_j + \sum_i \boldsymbol{\mu}_i \boldsymbol{\mu}_i/(2\alpha_i^2)$ is the potential energy due to the induced dipoles. Equation A1 leads to the equation of motion of the dipole degree of freedom, that is

$$m_{\mu,i}\ddot{\boldsymbol{\mu}}_i = -\boldsymbol{\mu}_i/\alpha_i + \boldsymbol{E}_i^0 + \sum_j \boldsymbol{T}_{ij}\boldsymbol{\mu}_j \tag{A2}$$

where $m_{\mu,i}$ is the fictitious mass to be specified. Note that the coupling between dipole and nuclear degrees of freedom is introduced through the second and the third terms in the above equation. A noninteracting model may be defined by $m_{\mu,i}\ddot{\boldsymbol{\mu}}_i = -\boldsymbol{\mu}_i/\alpha_i$, that is, a harmonic oscillator with the characteristic frequency

$$\omega_i = \frac{1}{2\pi}\sqrt{\frac{1}{\alpha_i m_{\mu,i}}} \tag{A3}$$

In the implementation of the above equations, it is desirable to have a small $m_{\mu,i}$ to make the induced dipole change "instantaneously" as the system propagates in time to satisfy the Born−Oppenheimer condition. In the MD simulation, it is adequate to assign a $m_{\mu,i}$ small enough to make ω_i larger than the highest frequency in the real system, while still keeping a reasonable integration time step. A too large $m_{\mu,i}$ can make the evolution of the dipole degrees of freedom lag behind the real system degrees of freedom and act as a friction slowing down the relaxation, thus "freezing" the system; this is a problem shared with the iterative method using a loose convergence criterion. However, a too small $m_{\mu,i}$ can make the induced dipoles propagate too fast and the system "blow up" if an inappropriate integration time step is used.[109] By keeping the fast dipole degrees of freedom (i.e., small fictitious mass with a proper integration time step) at a much lower temperature (i.e., coupled to a low temperature thermostat) with respect to the slowly evolving nuclear degrees of freedom, the classical adiabatic separation ensures that the fast degrees of freedom are "locked" on the Born−Oppenheimer potential energy surface.[122] Alternatively, the dipole degrees of freedom can be coupled to a Nosé-Hoover thermostat[113] at low temperature (i.e., 0.1 K) to keep them evolving on the adiabatic surface,[122] as implemented in our previous studies.[63,103,105]

Three simulations with the iteration method were performed. One had a very tight convergence criterion of $\delta\mu^{(n)} = [1/N\sum_{i=1}^{N}(\boldsymbol{\mu}_i^{(n)} - \boldsymbol{\mu}_i^{(n-1)})^2]^{1/2} \leq 10^{-8}$ Debye, another had a tight criterion of $\delta\boldsymbol{\mu}^{(n)} \leq 10^{-6}$ Debye, and the other had a loose criterion of $\delta\boldsymbol{\mu}^{(n)} \leq 10^{-4}$ Debye, respectively, with n number of iterations, and N number of polarization centers in the system. The production run in this work utilized the ext-L with $m_{\mu,i} = 2.4 \times 10^{-7}/\alpha_i$ (in units of $\text{Å}^{-3}\text{ps}^2$), corresponding to a characteristic frequency $\omega_i = 10829\ \text{cm}^{-1}$ (vibrational period ~3.1 fs) for each of the N induced dipoles using eq A3. Thus, the dipole degrees of freedom were much faster than the nuclear degrees of freedom.[122] The long-range electrostatic interactions were handled with the Ewald sum. The cutoff distance was 12 Å for both the real part of the Ewald sum and the van der Waals interactions. For the ext-L run, the induced dipoles of the very first integration time step were calculated with the iteration method. The run time for the tests with iteration method was 1 ns with an integration time step of 1.0 fs, which was about one-eighth of the fastest dipole characteristic motions. The ext-L method does not require any iterations by virtue of its dipole degrees of freedom time propagation. In contrast, the iterative method required an average of 20−30 iterations for the convergence criterion of $\delta\boldsymbol{\mu}^{(n)} \leq 10^{-8}$ Debye, 15−20 iterations for $\delta\boldsymbol{\mu}^{(n)} \leq 10^{-6}$ Debye, and 10−15 iterations for $\delta\boldsymbol{\mu}^{(n)} \leq 10^{-4}$ Debye. Not surprisingly, the simulation utilizing the ext-L method ran much faster than the iteration method.

In contrast to our previous studies[63,103,105] in which the simulations with the polarizable models were run with the constant NVT simulation with the nuclear degrees of freedom coupled to a 400 K Nosé-Hoover thermostat[112,113] and the dipole degrees of freedom coupled to another Nosé-Hoover thermostat[112,113] with a much lower temperature (0.1 K),[122] all the simulations in this study were performed with the constant NVE ensemble (i.e., no thermostats). The total energy and temperature of the systems with the iteration method are shown in Figure 15a,b and those for the ext-L method are shown in Figure 15c,d, respectively. Total energy and temperature drifted significantly for the iteration method with the convergence criterion $\delta\boldsymbol{\mu}^{(n)} \leq 10^{-4}$ Debye. This is attributed to the evolution of the induced dipoles lagging behind the system nuclear evolution. This "electron friction" dissipates the energy into the electronic degrees of freedom and cools down the system, resulting in a negative energy drift. There were also small energy and temperature drifts for the convergence criterion $\delta\boldsymbol{\mu}^{(n)} \leq 10^{-6}$ Debye. The tight convergence criterion of $\delta\boldsymbol{\mu}^{(n)} \leq 10^{-8}$ Debye had essentially no energy or temperature drift, but the computational demand was much higher. For the ext-L method with fictitious dipole mass $m_{\mu,i} = 2.4 \times 10^{-7}/\alpha_i$, the total energy drifted down about 1 kcal/mol out of a total energy of ca. −11089 kcal/mol at time 0, that is, the energy drifted less than 0.01% in 10 ns, as shown in Figure 15c. Therefore, the total energy was well conserved over 10 ns of MD simulation for the ext-L method. Since constant *NVE* simulations were incorporated in this study, there was no thermostat coupled to either nuclear or dipole degrees of freedom. Nevertheless, the two types of degrees of freedom were apparently slightly coupled with each other. At the end of the 10 ns simulation, the dipole degrees of freedom heated up 2.3 K, as shown in Figure 15d. Ideally, the temperature of the dipole degrees of freedom should be 0 K as the dipoles evolve on the adiabatic surface. Since the dipole temperature was cool compared to the system temperature of 400 K during the 10 ns

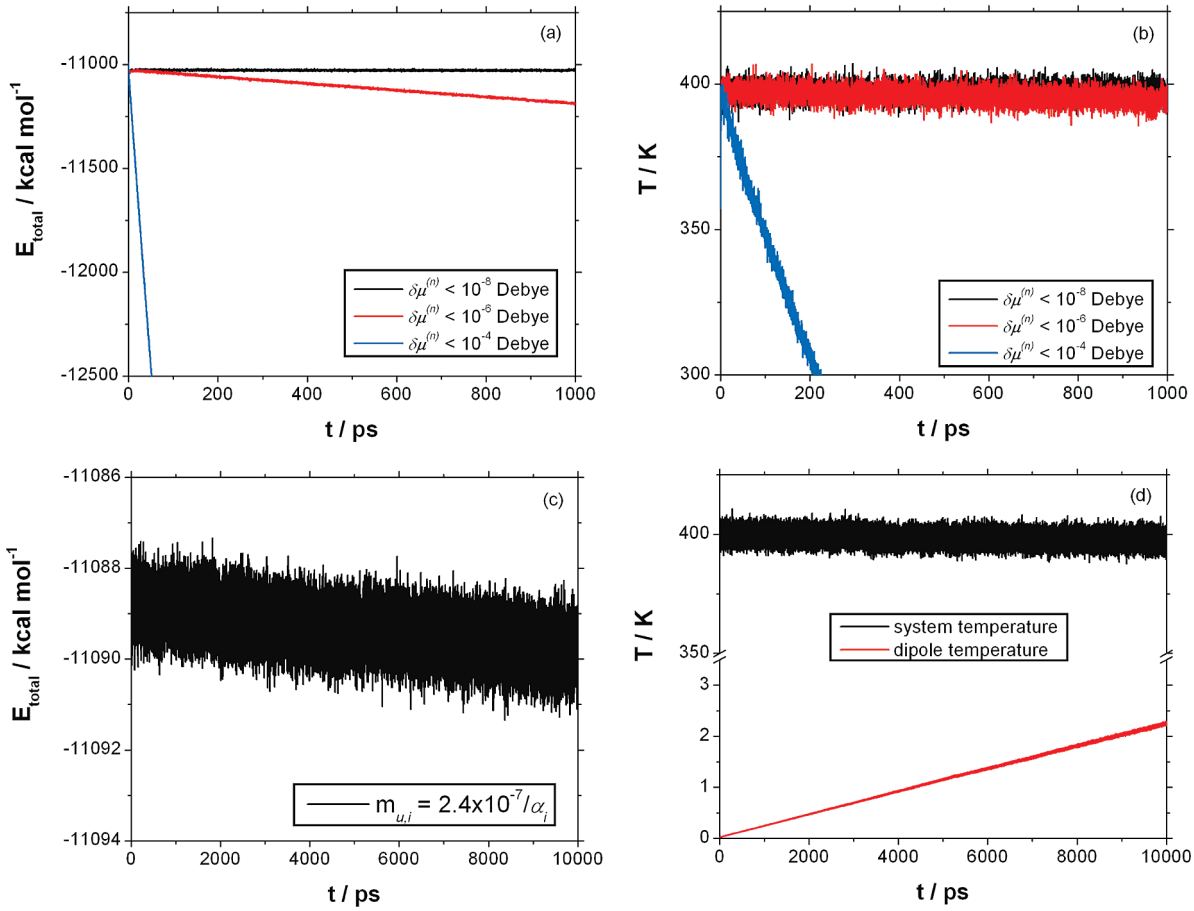

Figure 15. Comparisons of the simulations with the polarizable model, three of them utilize the iteration method for the dipole degrees of freedom, with the convergence criteria $\delta\boldsymbol{\mu}^{(n)} \leq 10^{-8}$, $\delta\boldsymbol{\mu}^{(n)} \leq 10^{-6}$, and $\delta\boldsymbol{\mu}^{(n)} \leq 10^{-4}$ Debye, respectively, and the other utilizes the ext-L method for the dipole degrees of freedom with a fictitious dipole mass $m_{\mu,i} = 2.4 \times 10^{-7}/\alpha_i$. The simulations with the iteration method were run for 1 ns each, and that for the ext-L method was run for 10 ns. (a) Time evolution of the total system energy for the three simulations with the iteration method in black, red, and blue for $\delta\boldsymbol{\mu}^{(n)} \leq 10^{-8}$, $\delta\boldsymbol{\mu}^{(n)} \leq 10^{-6}$, and $\delta\boldsymbol{\mu}^{(n)} \leq 10^{-4}$Debye, respectively; (b) same as (a) except for system temperature; (c) time evolution of the total system energy with ext-L method; (d) same as (c) except for system temperature (black) and dipole temperature (red).

MD simulation, the system temperature is well maintained at 400 K with little cooling, as shown in Figure 15d. Thus, no correction for the dipole temperature drift was performed in this study. For longer simulation times, such a correction to bring the dipole degrees of freedom back to the adiabatic surface may be needed and can be easily done by coupling the dipole degrees of freedom to a 0.1 K Nosé-Hoover thermostat[63,103,105] or calculating converged dipoles iteratively every certain number of integration steps during MD simulation.

The distributions of the induced dipoles on the cation and anion for the polarizable model with both the iteration method and ext-L method, are shown in Figure 16. The dipole distributions from the ext-L run closely resemble the ones from the iteration run. Since the polarizability of $EMIM^+$ is larger than that of NO_3^-, as shown in Table 1, the induced dipole moment on $EMIM^+$ is larger. The average induced dipole moments are 0.85 and 0.37 D for $EMIM^+$ and NO_3^-, respectively. In the AIMD study of IL $DMIM^+/Cl^-$,[82] the electronic polarization of the ions were estimated via localized Wannier orbitals by comparing the dipole moment in bulk and in isolated gas phase. It was found that the net polarization induces on average 0.7 D on $DMIM^+$ and 0.5 D on Cl^- with a wide fluctuation in the distribution, comparable to the polarizable force field of $EMIM^+/NO_3^-$ employed in this study. Though in the above AIMD simulation the dipole moment of $DMIM^+$ comes from both geometrical and electronic distortion compared to that in the isolated gas phase, the dipole moment of Cl^- is

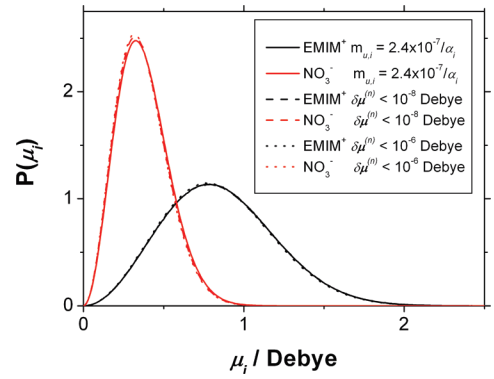

Figure 16. The induced dipole distributions on $EMIM^+$ (black) and NO_3^- (red) for the simulations of the polarizable model. Solid line, ext-L method with fictitious dipole mass $m_{\mu,i} = 2.4 \times 10^{-7}/\alpha_i$; dashed line, iteration method with convergence criterion $\delta\mu^{(n)} \leq 10^{-8}$ Debye; dotted line, iteration method with convergence criterion $\delta\boldsymbol{\mu}^{(n)} \leq 10^{-6}$ Debye.

solely caused by electronic distortion.[82] The PRDFs for the polarizable model with the iteration method and ext-L method, respectively, are also in good agreement, as shown in the Supporting Information.

Supporting Information Available: Figure S1 compares the PRDFs of the polarizable model with both the iteration method and ext-L method for the dipole degrees of freedom,

respectively, and those of the nonpolarizable model. The complete reference of 102. This material is available free of charge via the Internet at http://pubs.acs.org.

References and Notes

(1) Rogers, R. D.; Seddon, K. R. *Science* **2003**, *302*, 792.

(2) (a) Dupont, J.; Suarez, P. A. Z. *Phys. Chem. Chem. Phys.* **2006**, *8*, 2441. (b) Weingärtner, H. *Angew. Chem., Int. Ed.* **2008**, *47*, 654. (c) Haumann, M.; Riisager, A. *Chem. Rev.* **2008**, *108*, 1474.

(3) Rogers, R. D.; Voth, G. A. *Acc. Chem. Res.* **2007**, *40*, 1077.

(4) Hardacre, C.; Holbrey, J. D.; Jane McMath, S. E.; Bowron, D. T.; Soper, A. K. *J. Chem. Phys.* **2003**, *118*, 273.

(5) Hardacre, C.; Jane McMath, S. E.; Nieuwenhuyzen, M.; Bowron, D. T.; Soper, A. K. *J. Phys.: Condens. Matter* **2003**, *15*, S159.

(6) Deetlefs, M.; Hardacre, C.; Nieuwenhuyzen, M.; Pádua, A. A. H.; Sheppard, O.; Soper, A. K. *J. Phys. Chem. B* **2006**, *110*, 12055.

(7) Hardacre, C.; Holbrey, J. D.; Mullan, C. L.; Nieuwenhuyzen, M.; Youngs, T. G. A.; Bowron, D. T. *J. Phys. Chem. B* **2008**, *112*, 8049.

(8) Soper, A. K. *Chem. Phys.* **1996**, *202*, 295.

(9) Hanke, C. G.; Price, S. L.; Lynden-Bell, R. M. *Mol. Phys.* **2001**, *99*, 801.

(10) Wilkes, J. S.; Zaworotko, M. J. *J. Chem. Soc., Chem. Commun.* **1992**, 965.

(11) Kölle, P.; Dronskowski, R. *Inorg. Chem.* **2004**, *43*, 2803.

(12) Jodry, J. J.; Mikami, K. *Tetrahedron Lett.* **2004**, *45*, 4429.

(13) Huang, J.-F.; Chen, P.-Y.; Sun, I.-W.; Wang, S. P. *Spectrosc. Lett.* **2001**, *34*, 591.

(14) (a) Antony, J. H.; Mertens, D.; Breitenstein, T.; Dölle, A.; Wasserscheid, P.; Carper, W. R. *Pure Appl. Chem.* **2004**, *76*, 255. (b) de Andrade, J.; Böes, E. S.; Stassen, H. *J. Phys. Chem. B.* **2009**, *113*, 7541.

(15) Bühl, M.; Chaumont, A.; Schurhammer, R.; Wipff, G. *J. Phys. Chem. B* **2005**, *109*, 18591.

(16) Dieter, M. K.; Dymek, C. J., Jr.; Heimer, N. E.; Rovang, J. W.; Wilkes, J. S. *J. Am. Chem. Soc.* **1988**, *110*, 2722.

(17) (a) Wang, Y.; Li, H.; Han, S. *J. Chem. Phys.* **2005**, *123*, 174501. (b) Wang, Y.; Li, H.; Han, S. *J. Chem. Phys.* **2006**, *124*, 044504.

(18) Tsuzuki, S.; Tokuda, H.; Hayamizu, K.; Watanabe, M. *J. Phys. Chem. B* **2005**, *109*, 16474.

(19) Chang, H.-C.; Jiang, J.-C.; Tsai, W.-C.; Chen, G.-C.; Lin, S. H. *J. Phys. Chem. B* **2006**, *110*, 3302.

(20) () Wulf, A.; Fumino, K.; Michalik, D.; Ludwig, R. *ChemPhysChem.* **2007**, *8*, 2265. (b) Fumino, K.; Wulf, A.; Ludwig, R. *Angew. Chem., Int. Ed.* **2008**, *47*, 3830.

(21) Del Pópolo, M. G.; Lynden-Bell, R. M.; Kohanoff, J. *J. Phys. Chem. B* **2005**, *109*, 5895.

(22) Qiao, B.; Krekeler, C.; Berger, R.; Site, L. D.; Holm, C. *J. Phys. Chem. B* **2008**, *112*, 1743.

(23) Umebayashi, Y.; Fujimori, T.; Sukizaki, T.; Asada, M.; Fujii, K.; Kanzaki, R.; Ishiguro, S. *J. Phys. Chem. A* **2005**, *109*, 8976.

(24) Margulis, C. J.; Stern, H. A.; Berne, B. J. *J. Phys. Chem. B* **2002**, *106*, 12017.

(25) Del Pópolo, M. G.; Voth, G. A. *J. Phys. Chem. B* **2004**, *108*, 1744.

(26) Canongia Lopes, J. N.; Pádua, A. A. H. *J. Phys. Chem. B* **2006**, *110*, 7485.

(27) Hamaguchi, H.; Ozawa, R. *In Advances in Chemical Physics*; John Wiley & Sons, Inc.: New York, 2005; Vol. 131, pp 85.

(28) Fujii, K.; Fujimori, T.; Takamuku, T.; Kanzaki, R.; Umebayashi, Y.; Ishiguro, S. *J. Phys. Chem. B* **2006**, *110*, 8179.

(29) Katsyuba, S. A.; Zvereva, E. E.; Vidiš, A.; Dyson, P. J. *J. Phys. Chem. A* **2007**, *111*, 352.

(30) Wang, Y.; Voth, G. A. *J. Am. Chem. Soc.* **2005**, *127*, 12192.

(31) Wang, Y.; Voth, G. A. *J. Phys. Chem. B* **2006**, *110*, 18601.

(32) Wang, Y.; Jiang, W.; Yan, T.; Voth, G. A. *Acc. Chem. Res.* **2007**, *40*, 1193.

(33) Izvekov, S.; Parrinello, M.; Burnham, C. J.; Voth, G. A. *J. Chem. Phys.* **2004**, *120*, 10896.

(34) Wang, Y.; Izvekov, S.; Yan, T.; Voth, G. A. *J. Phys. Chem. B* **2006**, *110*, 3564.

(35) Rebelo, L. P. N.; Canongia Lopes, J. N.; Esperança, J. M. S. S.; Guedes, H. J. R.; £achwa, J.; Najdanovic-Visak, V.; Visak, Z. P. *Acc. Chem. Res.* **2007**, *40*, 1114.

(36) (a) Canongia Lopes, J. N.; Costa Gomes, M. F.; Pádua, A. A. H. *J. Phys. Chem. B.* **2006**, *110*, 16816. (b) Pádua, A. A. H.; Costa Gomes, M. F.; Canongia Lopes, J. N. *Acc. Chem. Res.* **2007**, *40*, 1087.

(37) Wang, Y.; Jiang, W.; Voth, G. A. In *Ionic Liquids IV Not Just Solvents Anymore*; Brennecke, J. F., Rogers, R. D., Kenneth, R., Eds.; ACS Symposium Series 975; American Chemical Society: Washington, DC, 2007.

(38) Bhargava, B. L.; Devane, R.; Klein, M. L.; Balasubramanian, S. *Soft Matter* **2007**, *3*, 1395.

(39) Chiappe, C. *Monatsh. Chem.* **2007**, *138*, 1035.

(40) (a) Xiao, D.; Rajian, J. R.; Li, S.; Bartsch, R. A.; Quitevis, E. L. *J. Phys. Chem. B.* **2006**, *110*, 16174. (b) Xiao, D.; Rajan, J. R.; Cady, A.; Li, S.; Bartsch, R. A.; Quitevis, E. L. *J. Phys. Chem. B* **2007**, *111*, 4669. (c) Xiao, D.; Rajian, J. R.; Hines, L. G., Jr.; S., L.; Bartsch, R. A.; Quitevis, E. L. *J. Phys. Chem. B* **2008**, *112*, 13316.

(41) (a) Shigeto, S.; Hamaguchi, H. *Chem. Phys. Lett.* **2006**, *427*, 329. (b) Iwata, K.; Okajima, H.; Saha, S.; Hamaguchi, H. *Acc. Chem. Res.* **2007**, *40*, 1174.

(42) (a) Triolo, A.; Russina, O.; Bleif, H. J.; Cola, E. D. *J. Phys. Chem. B.* **2007**, *111*, 4641. (b) Triolo, A.; Russina, O.; Fazio, B.; Triolo, R.; Cola, E. D. *Chem. Phys. Lett.* **2008**, *457*, 362.

(43) Pott, T.; Méléard, P. *Phys. Chem. Chem. Phys.* **2009**, *11*, 5469.

(44) Triolo, A.; Russina, O.; Fazio, B.; Appetecchi, G. B.; Carewska, M.; Passerini, S. *J. Chem. Phys.* **2009**, *130*, 164521.

(45) Russina, O.; Triolo, A.; Gontrani, L.; Caminiti, R.; Xiao, D.; Hines Jr, L. G.; Bartsch, R. A.; Quitevis, E. L.; Plechkova, N.; Seddon, K. R. *J. Phys.: Condens. Matter* **2009**, *21*, 424121.

(46) Atkin, R.; Warr, G. G. *J. Phys. Chem. B* **2008**, *112*, 4164.

(47) (a) Mandal, P. K.; Sarkar, M.; Samanta, A. *J. Phys. Chem. A.* **2004**, *108*, 9048. (b) Samanta, A. *J. Phys. Chem. B* **2006**, *110*, 13704.

(48) (a) Yamamoto, K.; Tani, M.; Hangyo, M. *J. Phys. Chem. B.* **2007**, *111*, 4854. (b) Turton, D.; Hunger, J.; Stoppa, A.; Hefter, G.; Thoman, A.; Walther, M.; Buchner, R.; Wynne, K. *J. Am. Chem. Soc.* **2009**, *131*, 11140.

(49) Ichikawa, T.; Yoshio, M.; Hamasaki, A.; Mukai, T.; Ohbo, H.; Kato, T. *J. Am. Chem. Soc.* **2007**, *129*, 10662.

(50) (a) Holbrey, J. D.; Reichert, W. M.; Nieuwenhuyzen, M.; Sheppard, O.; Hardacre, C.; Rogers, R. D. *Chem Commun* 2003. (b) Deetlefs, M.; Hardacre, C.; Nieuwenhuyzen, M.; Sheppard, O.; Soper, A. K. *J. Phys. Chem. B* **2005**, *109*, 1593. (c) Wu, J. J.; Li, N.; Li, K. A.; Liu, F. *J. Phys. Chem. B* **2008**, *112*, 8134.

(51) Tsuzuki, S.; Mikami, M.; Yamada, S. *J. Am. Chem. Soc.* **2007**, *129*, 8656.

(52) Wilkes, J. S.; Zaworotko, M. *J. Supramol. Chem.* **1993**, *1*, 191.

(53) Choudhury, A. R.; Winterton, N.; Steiner, A.; Cooper, A. I.; Johnson, K. A. *J. Am. Chem. Soc.* **2005**, *127*, 16792.

(54) Mele, A.; Romanó, G.; Giannone, M.; Ragg, E.; Fronza, G.; Raos, G.; Marcon, V. *Angew. Chem., Int. Ed.* **2006**, *45*, 1123.

(55) Li, H.; Boatz, J. A.; Gordon, M. S. *J. Am. Chem. Soc.* **2008**, *130*, 392.

(56) Hunt, P. A.; Gould, I. R. *J. Phys. Chem. A* **2006**, *110*, 2269.

(57) Micaelo, N. M.; Baptisa, A. M.; Soares, C. M. *J. Phys. Chem. B* **2006**, *110*, 14444.

(58) de Andrade, J.; Bö; es, E. S.; Stassen, H. *J. Phys. Chem. B.* **2008**, *112*, 8966.

(59) Bhargava, B. L.; Balasubramanian, S. *Chem. Phys. Lett.* **2006**, *417*, 486.

(60) (a) de Andrade, J.; Bö; es, E. S.; Stassen, H. *J. Phys. Chem. B* **2002**, *106*, 13344. (b) Margulis, C. J. *Mol. Phys.* **2004**, *102*, 829. (c) Shim, Y.; Choi, M. Y.; Kim, H. J. *J. Chem. Phys.* **2005**, *122*, 044510. (d) Shim, Y.; Choi, M. Y.; Kim, H. J. *J. Chem. Phys.* **2005**, *122*, 044511. (e) Urahata, S. M.; Ribeiro, M. C. C. *J. Chem. Phys.* **2005**, *122*, 024511. (f) Alavi, S.; Thompson, D. L. *J. Chem. Phys.* **2005**, *122*, 154704. (g) Alavi, S.; Thompson, D. L. *J. Phys. Chem. B* **2005**, *109*, 18127. (h) Bhargava, B. L.; Balasubramanian, S. *J. Chem. Phys.* **2005**, *123*, 144505. (i) Borodin, O.; Smith, G. D. *J. Phys. Chem. B* **2006**, *110*, 11481. (j) Agrawal, P. M.; Rice, B. M.; Zhang, L.; Velardez, G. F.; Thompson, D. L., *J. Phys. Chem. B* **2006**, *110*, 5721. (k) Hu, Z.; Margulis, C. J. *Proc. Natl. Acad. Sci. U.S.A.* **2006**, *103*, 831. (l) Hu, Z.; Margulis, C. J. *J. Phys. Chem. B* **2006**, *110*, 11025. (m) Urahata, S. M.; Ribeiro, M. C. C. *J. Chem. Phys.* **2006**, *124*, 074513. (n) Chang, T. M.; Dang, L. X. *J. Phys. Chem. A* **2009**, *113*, 2027.

(61) Morrow, T. I.; Maginn, E. J. *J. Phys. Chem. B* **2002**, *106*, 12807.

(62) Urahata, S. M.; Ribeiro, M. C. C. *J. Chem. Phys.* **2004**, *120*, 1855.

(63) Yan, T.; Burnham, C. J.; Del Pópolo, M. G.; Voth, G. A. *J. Phys. Chem. B* **2004**, *108*, 11877.

(64) Liu, Z.; Huang, S.; Wang, W. *J. Phys. Chem. B* **2004**, *108*, 12978.

(65) Canongia Lopes, J. N.; Deschamps, J.; Pádua, A. A. H. *J. Phys. Chem. B* **2004**, *108*, 2038.

(66) (a) Liu, Z.; Wu, X.; Wang, W. *Phys. Chem. Chem. Phys.* **2006**, *8*, 1096. (b) Liu, Z.; Chen, T.; Bell, A.; Smit, B. *J. Phys. Chem. B* **2010**, *114*, 4572.

(67) Wu, X.; Liu, Z.; Huang, S.; Wang, W. *Phys. Chem. Chem. Phys.* **2005**, *7*, 2771.

(68) (a) Cadena, C.; Zhao, Q.; Snurr, R. Q.; Maginn, E. J. *J. Phys. Chem. B.* **2006**, *110*, 2821. (b) Liu, X.; Zhang, S.; Zhou, G.; Wu, G.; Yuan, X.; Yao, X. *J. Phys. Chem. B* **2006**, *110*, 12062.

(69) (a) Canongia Lopes, J. N.; Deschamps, J.; H., P. A. A. *J. Phys. Chem. B* **2004**, *108*, 11250. (b) Canongia Lopes, J. N.; Pádua, A. A. H.; Shimizu, K. *J. Phys. Chem. B* **2008**, *112*, 5039. (c) Liu, X.; Zhang, S.; Zhou, G.; Wu, G.; Yu, X.; X., Y. *J. Phys. Chem. B* **2006**, *110*, 12062. (d) Liu, X.; Zhou, G.; Zhang, S.; Wu, G.; Yu, G. *J. Phys. Chem. B* **2007**, *111*, 5658. (e) Zhou, G.; Liu, X.; Zhang, S.; Yu, G.; He, H. *J. Phys. Chem. B* **2007**, *111*, 7078. (f) Sambasivarao, S. V.; Acevedo, O. *J. Chem. Theory*

Comput. **2009**, *5*, 1038. (g) Canongia Lopes, J. N.; Pádua, A. A. H. *J. Phys. Chem. B* **2004**, *108*, 16893. (h) Canongia Lopes, J. N.; Pádua, A. A. H. *J. Phys. Chem. B* **2006**, *110*, 19586. (i) Shimizu, K.; Almantariotis, D.; Costa Gomes, M. F.; Pádua, A. A. H.; Canongia Lopes, J. N. *J. Phys. Chem. B* **2010**, *114*, 3592.

(70) (a) Bhargava, B. L.; Balasubramanian, S. *J. Chem. Phys.* **2007**, *127*, 114510. (b) Youngs, T. G. A.; Hardacre, C. *ChemPhysChem* **2008**, *9*, 1548.

(71) Köddermann, T.; Paschek, D.; Ludwig, R. *ChemPhysChem* **2007**, *17*, 2464.

(72) Malvaldi, M.; Chiappe, C. *J. Phys.: Condens. Matter* **2008**, *20*, 035108.

(73) (a) Jiang, W.; Wang, Y.; Yan, T.; Voth, G. A. *J. Phys. Chem. C* **2008**, *112*, 1132. (b) Bedrov, D.; Borodin, O.; Li, Z.; Smith, G. D. *J. Phys. Chem. B* **2010**, *114*, 4984.

(74) Hunt, P. A.; Kirchner, B.; Welton, T. *Chem.—Eur. J.* **2006**, *12*, 6762.

(75) Schröder, C.; Steinhauser, O. *J. Chem. Phys.* **2008**, *128*, 224503.

(76) Hunt, P. A. *Mol. Simul.* **2006**, *32*, 1.

(77) Bhargava, B. L.; Balasubramanian, S.; Klein, M. L. *Chem. Commun.* 2008.

(78) Gray-Weale, A. *Aust. J. Chem.* **2009**, *62*, 288.

(79) Maginn, E. J. *J. Phys.: Condens. Matter* **2009**, *21*, 373101.

(80) Kowsari, M. H.; Alavi, S.; Ashrafizaadeh, M.; Najafi, B. *J. Chem. Phys.* **2008**, *129*, 224508.

(81) (a) Del Pópolo, M. G.; Kohanoff, J.; Lynden-Bell, R. M. *J. Phys. Chem. B* **2006**, *110*, 8798. (b) Thar, J.; Brehm, M.; Seitsonen, A. P.; Kirchner, B. *J. Phys. Chem. B* **2009**, *113*, 15129.

(82) Prado, C. E. R.; Del Pópolo, M. G.; Youngs, T. G. A.; Kohanoff, J.; Lynden-Bell, R. M. *Mol. Phys.* **2006**, *104*, 2477.

(83) Krekeler, C.; Dommert, F.; Schmidt, J.; Zhao, Y. Y.; Holm, C.; Berger, R.; Delle Site, L. *Phys. Chem. Chem. Phys.* **2010**, *12*, 1817.

(84) Youngs, T. G. A.; Del Pópolo, M. G.; Kohanoff, J. *J. Phys. Chem. B* **2006**, *110*, 5697.

(85) Wilson, M.; Madden, P. A. *Phys. Rev. Lett.* **1996**, *77*, 4023.

(86) Madden, P. A.; Wilson, M. *J. Phys.: Condens. Matter* **2000**, *12*, A95.

(87) Saboungi, M.-L.; Rahman, A.; Halley, J. W.; Blander, M. *J. Chem. Phys.* **1988**, *88*, 5818.

(88) Wilson, M.; Madden, P. A. *Mol. Phys.* **1997**, *92*, 197.

(89) (a) Hutchinson, F.; Rowley, A. J.; Walters, M. K.; Wilson, M.; Madden, P. A.; Wasse, J. C.; Salmon, P. S. *J. Chem. Phys.* **1999**, *111*, 2028. (b) Morgan, B.; Madden, P. A. *J. Chem. Phys.* **2004**, *120*, 1402.

(90) Ribeiro, M. C. C. *J. Phys. Chem. B* **2003**, *107*, 9520.

(91) Jacucci, G.; McDonald, I. R.; Rahman, A. *Phys. Rev. A* **1976**, *13*, 1581.

(92) Lynden-Bell, R. M.; Del Pópolo, M. G.; Youngs, T. G. A.; Kohanoff, J.; Hanke, C. G.; Harper, J. B.; Pinilla, C. C. *Acc. Chem. Res.* **2007**, *40*, 1138.

(93) (a) Kobmann, S.; Thar, J.; Kirchner, B.; Hunt, P. A.; Welton, T. *J. Chem. Phys.* **2006**, *124*, 174506. (b) Zorn, D. D.; Boatz, J. A.; Gordon, M. S. *J. Phys. Chem. B* **2006**, *110*, 11110.

(94) Hardacre, C.; Holbrey, J. D.; Nieuwenhuyzen, M.; Youngs, T. G. A. *Acc. Chem. Res.* **2007**, *40*, 1146.

(95) Stone, A. J. *The Theory of Intermolecular Forces*; Oxford University Press: Oxford, 1996.

(96) Gray-Weale, A.; Madden, P. A. *Mol. Phys.* **2003**, *101*, 1761.

(97) Applequist, J.; Carl, J. R.; Fung, K.-K. *J. Am. Chem. Soc.* **1972**, *94*, 2952.

(98) Thole, B. T. *Chem. Phys.* **1981**, *59*, 341.

(99) Burnham, C. J.; Li, J.; Xantheas, S. S. *J. Chem. Phys.* **1999**, *110*, 4566.

(100) Yan, T.; Wang, Y.; Knox, C. *J. Phys. Chem. B.* [Online early release.] DOI: jp908914d.

(101) van Duijnen, P. T.; Swart, M. *J. Phys. Chem. A* **1998**, *102*, 2399.

(102) Frisch, M. J.; Trucks, G. W.; Schlegel, H. B.; et al. *Gaussian 03*, C. 01; Gaussian, Inc.: Wallingford, CT, 2004.

(103) Yan, T.; Li, S.; Jiang, W.; Gao, X. P.; Xiang, B.; Voth, G. A. *J. Phys. Chem. B* **2006**, *110*, 1800.

(104) (a) Bayly, C. I.; Cieplak, P.; Cornell, W. D.; Kollman, P. A. *J. Phys. Chem.* **1993**, *97*, 10269. (b) Cornell, W. D.; Cieplak, P.; Bayly, C. I.; Kollman, P. A. *J. Am. Chem. Soc.* **1993**, *115*, 9620.

(105) Jiang, W.; Yan, T.; Wang, Y.; Voth, G. A. *J. Phys. Chem. B* **2008**, *112*, 3121.

(106) Smith, W.; Forester, T. R. The DL_POLY Molecular Simulation Package; http://www.dl.ac.uk/TCSC/Software/DL_POLY/main.html, 1999.

(107) Smith, W. *Comput. Phys. Commun.* **1992**, *67*, 392.

(108) (a) Smith, W. *CCP5 Information Quarterly.* **1982**, *4*, 13. (b) Nymand, T. M.; Linse, P. *J. Chem. Phys.* **2000**, *112*, 6152. (c) Aguado, A.; Madden, P. A. *J. Chem. Phys.* **2003**, *119*, 7471.

(109) Toukmaji, A.; Sagui, C.; Board, J.; Darden, T. *J. Chem. Phys.* **2000**, *113*, 10913.

(110) Cornell, W. D.; Cieplak, P.; Bayly, C. I.; Gould, I. R.; Merz, K. M. J.; Ferguson, D. M.; Spellmeyer, D. C.; Fox, T.; Caldwell, J. W.; Kollman, P. A. *J. Am. Chem. Soc.* **1995**, *117*, 5179.

(111) Melchionna, P.; Cicocoti, G.; Holian, B. *Mol. Phys.* **1993**, *78*, 533.

(112) Nosé, S. *J. Chem. Phys.* **1984**, *81*, 511.

(113) Hoover, W. G. *Phys. Rev. A* **1985**, *31*, 1695.

(114) (a) Lynden-Bell, R. M. *Electrochem. Commun.* **2007**, *9*, 1857. (b) Lynden-Bell, R. M. *J. Phys. Chem. B* **2007**, *111*, 10800. Lynden-Bell, R. M. *J. Chem. Phys.* **2008**, *129*, 204503. (c) Streeter, I.; Lynden-Bell, R. M.; Compton, R. G. *J. Phys. Chem. B* **2008**, *112*, 14538.

(115) Lynden-Bell, R. M.; Young, T. G. A. *J. Phys.: Condens. Matter* **2009**, *21*, 424120.

(116) La Violette, R. A.; Budzien, J. L.; Stillinger, F. H. *J. Chem. Phys.* **2000**, *112*, 8072.

(117) Siqueira, L. J. A.; Ribeiro, M. C. C. *J. Phys. Chem. B* **2007**, *111*, 11776.

(118) Nakano, H.; Yamamoto, T.; Kato, S. *J. Chem. Phys.* **2010**, *132*, 044106.

(119) Katayanagi, H.; Hayashi, S.; Hamaguchi, H.; Nishikawa, K. *Chem. Phys. Lett.* **2004**, *392*, 460.

(120) (a) Kuo, J.-L.; Klein, M. L. *J. Chem. Phys.* **2005**, *122*, 024516. (b) Burnham, C. J.; Petersen, M. K.; Day, T. J. F.; Iyengar, S. S.; Voth, G. A. *J. Chem. Phys.* **2006**, *122*, 024327.

(121) Jiang, W.; Wang, Y.; Voth, G. A. *J. Phys. Chem. B* **2007**, *111*, 4812.

(122) Sprik, M. *J. Phys. Chem.* **1991**, *95*, 2283.

(123) Ahlström, P.; Wallqvist, A.; Engström, S.; Jöhnsson, B. *Mol. Phys.* **1989**, *68*, 563.

JP9089112